UNIVERSIDADE
BEIRA INTERIOR

Development of silica-coated gold nanoclusters for cancer therapy

Natanael Filipe Ferreira Fernandes

Dissertação para obtenção do Grau de Mestre em
Bioquímica
(2º ciclo de estudos)

Orientador: Prof. Doutor Ilídio Joaquim Sobreira Correia
Co-orientador: Doutor André Ferreira Moreira
Co-orientador: Mestre Ana Carolina Félix Rodrigues

setembro de 2020

“The scientist is not someone who gives the right answers but one who asks the right questions.”

Claude Lévi-Strauss

Dedication

Quero agradecer aos meus pais, irmãos e à Ana que me apoiaram e me incentivaram em todos os sentidos durante toda esta caminhada.

Acknowledgments

Primeiro, quero agradecer ao meu orientador Professor Ilídio Correia, por me ter deixado fazer parte do seu grupo de trabalho e provar que a exigência e a boa disposição andam sempre de mãos dadas. Agradeço a sua orientação exemplar marcada por um elevado e rigoroso nível científico, um interesse permanente, uma visão crítica e oportuna e um empenho inexcedível, os quais contribuíram para enriquecer, com grande dedicação, passo por passo, todas as etapas subjacentes ao trabalho realizado.

Ao meu co-orientador, André Moreira, agradeço toda a ajuda, paciência e por todo o tempo que despendeu comigo ao longo desta dissertação. Sem a sua orientação, apoio e confiança neste caminho percorrido até aqui, nada seria possível.

À minha co-orientadora Carolina, quero agradecer todo o conhecimento, tempo despendido e ajuda que me transmitiu. Mais uma vez obrigado pelo apoio e sabedoria que foram um pilar essencial para que este trabalho fosse possível!

Um obrigado a todo o grupo de investigação pela ajuda e disponibilidade que mostraram ao longo ano, em especial à Ariana e ao Miguel Leitão por me apoiarem em todos os momentos e por me ajudarem em tudo o que era preciso sem hesitar.

Aos meus parceiros Luís Brás, Emanuel Farinha e Júnior Gava quero agradecer o apoio infinito que me deram, por me ajudarem em tudo que precisei e não precisei. Levo no coração momentos inesquecíveis e espero manter contacto convosco para toda a vida.

À minha namorada Ana, quero agradecer pela força transmitida, pela paciência e pelo amor demonstrado em todo o caminho que já percorremos juntos. Agradecer-te não é um gesto que se põe em papel, mas algo que se partilha ao longo da vida.

Por fim, agradeço àqueles que me proporcionaram tudo isto. Aos meus pais quero agradecer todo apoio incondicional, pela força transmitida. À minha mãe quero também agradecer por nunca ter desistido de mim, sem ti, sem os teus conhecimentos, sem a tua força de vontade talvez não tivesse chegado onde cheguei hoje. Aos meus irmãos quero agradecer todo o amor e apoio que me deram e continuam a dar apesar da distância. E por fim, quero agradecer aos meus padrinhos todo o carinho, apoio e por serem como meus segundos pais.

Resumo

O cancro é uma das principais causas de morte da população mundial. Atualmente os tratamentos usados no tratamento desta doença, como sejam a cirurgia, radioterapia e quimioterapia, apresentam uma baixa eficiência terapêutica e apresentam efeitos secundários adversos para os pacientes. Esta realidade tem estimulado os investigadores a desenvolverem novas abordagens terapêuticas mais eficazes, como a imunoterapia, terapia genética e hipertermia.

Na área da hipertermia, a aplicação de nanomateriais para mediar um efeito fototérmico (ou seja, produção de calor em resposta a um estímulo de luz) e a consequente morte de células cancerígenas tem sido objeto de diversos estudos realizados por investigadores e profissionais de saúde. Dentro dos diversos tipos de nanopartículas desenvolvidas até o momento, as nanopartículas de ouro revestidas com sílica mesoporosa (AuMSS) apresentam excelentes propriedades físicas, químicas e biológicas, que são compatíveis com a sua aplicação como agentes fototérmicos e transportadores de fármacos. No entanto, a aplicação de nanopartículas de ouro esféricas na terapia fototérmica do cancro é dificultada pela sua baixa absorção na região do infravermelho próximo (NIR).

O plano de trabalho desenvolvido nesta dissertação teve como objetivo produzir e otimizar a síntese de AuMSS, constituídas por um núcleo formado por nanoagregados de esferas de ouro, com uma morfologia que lhes permite incrementar a sua absorção na região do NIR. Uma maior absorção na região do NIR permite a estes nanoagregados produzir uma maior variação de temperatura nos tecidos tumorais, e por consequência serem utilizados como agentes fototerapêuticos.

Os resultados obtidos neste estudo revelaram que a glutationa (GSH) pode ser utilizada para mediar a agregação de nanoesferas de ouro com uma morfologia uniforme com diversos núcleos de ouro e um revestimento de sílica bem definidos. Esta otimização da agregação das nanoesferas de ouro permitiu incrementar a sua capacidade fototérmica, induzindo alterações no espectro de absorção na região NIR. Nos ensaios *in vitro* foi demonstrada a biocompatibilidade de todas as formulações produzidas até concentrações de 200 μg/mL, quando estas foram colocadas em contacto com células saudáveis (fibroblastos) e cancerígenas (células do cancro do colo do útero). Por outro lado, o efeito fototérmico mediado pelos nanoagregados de AuMSS induziu um efeito citotóxico nas células cancerígenas.

Em suma, os resultados obtidos confirmam o potencial destes nanodispositivos para aplicação na terapia do cancro, onde futuramente poderão ser usados como agentes teragnósticos, *i.e.* agentes de entrega de fármacos e de imagiologia.

Palavras-chave

Cancro; nanopartículas de ouro com revestimento de sílica; terapia fototérmica; nanoagregados; glutationa

Resumo alargado

Na atualidade, o cancro é uma das doenças com maior impacto na saúde pública a nível mundial. As elevadas taxas de incidência e de mortalidade associadas a esta doença devem-se, em grande parte, à falta de eficácia dos tratamentos atualmente usados em meio clínico, como a radioterapia, cirurgia e quimioterapia. A quimioterapia é a abordagem terapêutica mais utilizada na clínica, no entanto esta apresenta diversas desvantagens relacionadas com a falta de especificidade e rápida degradação dos fármacos quimioterapêuticos, o que leva a que estes agentes tenham uma baixa biodisponibilidade. Devido a este facto, são administradas doses elevadas de fármacos aos pacientes, o que na maioria dos casos, tem efeitos secundários. Este cenário evidencia a necessidade de desenvolver novas abordagens terapêuticas mais eficazes para o cancro.

Os avanços na área da nanotecnologia permitiram o desenvolvimento de sistemas à escala nanométrica (nanopartículas) capazes de superar as diversas limitações associadas às terapias convencionais. De facto, a fototerapia mediada por nanomateriais tem sido objeto de diversos estudos realizados por investigadores e profissionais de saúde. Este tipo de abordagem terapêutica aproveita a capacidade intrínseca das nanopartículas de se acumularem no tecido tumoral e de produzirem calor quando irradiadas com um comprimento de onda específico, diminuindo assim os efeitos secundários nos tecidos saudáveis. Este aumento localizado de temperatura pode causar danos irreversíveis ao tecido tumoral, levando à sua destruição. Para além disso, para garantir que a ativação das nanopartículas tem o menor impacto possível nos tecidos saudáveis, é utilizada luz com um comprimento de onda no infravermelho próximo ((NIR), *i.e.* 750-1000 nm) do espectro eletromagnético. Esta radiação apresenta uma baixa interação com os componentes biológicos (*e.g.* sangue, músculos e água), o que também garante uma elevada capacidade de penetração nos tecidos. Assim, os nanomateriais utilizados na terapia fototérmica devem ter capacidade para absorver na região do NIR.

Entre os diferentes tipos de nanopartículas em desenvolvimento, as nanoparticulas com núcleo de ouro revestidas com sílica mesoporosa esféricas têm sido amplamente estudadas para aplicação na área do cancro, devido às suas propriedades físico-químicas que permitem sua aplicação não só no transporte de fármacos, mas também na imagiologia. Para a sua utilização na terapia fototérmica, as nanopartículas de ouro esféricas têm de ser organizadas em “shells” e / ou nanoagregados de nanopartículas.

O plano de trabalho realizado no âmbito desta dissertação teve como objetivo projetar, produzir e otimizar a síntese de AuMSS, constituídas por um núcleo formado por nanoagregados de esferas de ouro, para potenciar o efeito fototérmico das nanopartículas de ouro esféricas. Para este propósito, a glutationa (GSH) foi utilizada para promover a agregação das nanopartículas esféricas, que posteriormente foram revestidas com sílica mesoporosa. Neste processo foi otimizada tanto a concentração da GSH bem como da fonte de sílica o ortosilicato de tetraetilo (TEOS) levando à formação de diversas formulações de nanoagregados denominados Formulação A, B, C, D, E, F, G, H e I. Estas modificações foram realizadas para alcançar uma morfologia que permite incrementar a absorção das AuMSS na região do NIR.

Os resultados obtidos neste estudo revelaram que a GSH pode ser utilizada para mediar a agregação de nanoesferas de ouro com sucesso, e as AuMSS produzidas exibiam uma morfologia uniforme com diversos núcleos de ouro e um revestimento de sílica bem definidos. Esta agregação das nanoesferas de ouro permitiu incrementar a capacidade dos nanoagregados de AuMSS interagirem com a radiação do NIR. Esta interacção foi confirmada através da aquisição dos espectros de absorção onde se observou uma deslocação do pico de absorção da região visível para a região do NIR. Além disso, também se verificou um aumento da capacidade de absorção na região de 700-800 nm em comparação com as nanoesferas de ouro. As duas melhores conformações de nanoagregados (Formulação H e I) apresentaram um potencial zeta com valores negativos (-30,5±5,95 e -25,6±5 mV). Esta carga superficial negativa dos nanoagregados é atribuída aos grupos de silano presentes na superfície da partícula, demonstrando o correto revestimento com sílica. De acordo com o seu espectro de absorção, os nanoagregados de AuMSS foram capazes de mediar a produção de calor em resposta à radiação com luz NIR, tendo sido detetado o maior aumento de temperatura, $\Delta T = 20$ ^{o}C, com a formulação H. Nos ensaios *in vitro* foi ainda demonstrada a biocompatibilidade de todas as formulações até concentrações máximas de 200 μg/mL. Por fim, o efeito fototérmico mediado pelos nanoagregados de AuMSS induziu a morte das células cancerígenas. A formulação H foi capaz de induzir a diminuição da viabilidade celular, após 3 irradiações com luz NIR, para valores abaixo dos 25%. Entre todas as formulações testadas, a formulação H foi a que apresentou os resultados físico-químicos e biológicos mais promissores.

Em suma, os resultados apresentados nesta dissertação confirmam a correta agregação das nanopartículas de ouro esféricas e o seu potencial para aplicação na terapia do cancro, onde futuramente poderão ser usados simultaneamente para a entrega de fármacos, fototerapia e imagiologia.

Abstract

Cancer is one of the leading causes of death worldwide. Currently, the conventional treatments used in the clinic such as surgery, radiotherapy, and chemotherapy have a low therapeutic efficiency and adverse side effects on patients. This reality has propelled researchers to develop new and more effective therapeutic approaches such as immunotherapy, gene therapy, and hyperthermia.

In the area of hyperthermia, the application of nanomaterials to mediate a photothermal effect (*i.e.*, heat production in response to a light stimulus) and the consequent death of cancer cells has been the subject of several studies conducted by researchers and health professionals. Among the different types of nanoparticles developed up to date, gold nanoparticles coated with mesoporous silica (AuMSS) present excellent physical, chemical, and biological properties to be applied as photothermal agents and drug carriers. However, the application of spherical gold nanoparticles in the photothermic therapy of cancer is hampered by their low absorption in the near infrared (NIR) region.

The work plan developed in this MSc dissertation aimed to produce and optimize the synthesis of AuMSS, composed of a core of gold nanospheres nanocluster, with an ideal morphology that is able to increase their absorption in the NIR region. With the increment of their absorption in the NIR region, allow them to produce an increase of temperature in the tumor tissues and, consequently, to be used as phototherapeutic agents.

The obtained results revealed that the aggregation of gold nanospheres mediated by glutathione (GSH) was successful and the nanomaterials exhibited an uniform morphology with several gold nuclei and a well-defined silica coating. The optimization of the clustering of gold nanospheres allowed to improve their photothermal capacity, inducing changes in their absorption spectra, particularly, in the NIR region, as already expected. In the *in vitro* tests, all the formulations demonstrated to be biocompatible with both healthy (fibroblasts) and carcinogenic (cervical cancer) cells even when maximum concentrations of 200 μg/mL were used. Finally, the photothermic effect mediated by AuMSS nanoclusters effectively induced the death of cervical cancer cells.

In summary, the obtained results confirm the potential of the AuMSSs to be applied in cancer therapy, where in the near future they canceragnostic agents, *i.e.* drug delivery and imaging agents.

Keywords

Cancer; gold Core silica shell nanoparticles; photothermal therapy; nanoclusters; glutathione

List of Publications

Article published in international peer-reviewed journals:

Fernandes, N.F., Rodrigues, C.F., Moreira, A. F., and Correia, I. J. (2020). "*Overview of the application of inorganic nanomaterials in cancer photothermal therapy*." Biomaterials science. 8: 2990-3020. DOI: https://doi.org/10.1039/D0BM00222D

Index

Figure Index

List of Abbreviations

ANOVA	Analysis of Variance
AR	Aspect Ratio
AuMSS	Gold-core Mesoporous Silica Shell
BSA	Bovine Serum Albumin
CLSM	Confocal Laser Scanning Microscopy
CTAB	Hexadecyltrimethylammonium Bromide
Cy5.5	Cyanine Dye
DLS	Dynamic Light Scattering
DMEM-F12	Dulbecco's Modified Eagle Medium/Nutrient Mixture F-12
DMEM-HG	Dulbecco's Modified Eagle Medium-High Glucose
DOX	Doxorubicin
EPR	Enhanced Permeability and Retention
EtOH	Ethanol
FA	Folic Acid
FibH	Human Fibroblasts
GSH	Glutathione
HA	Hyaluronic Acid
HeLa	Human Negroid Cervix Epithelioid Carcinoma
K-	Negative Control
K+	Positive Control
L	Length
MS	Mesoporous Silica
NIR	Near Infrared
PBS	Phosphate-Buffered Saline
PEG	Poly(ethylene glycol)
PEI	Poly(ethyleneimine)
PI	Propidium Iodide
PTT	Photothermal Therapy
SPR	Surface Plasmon Resonance
TEM	Transmission Electron Microscopy
TEOS	Tetraethyl Orthosilicate
THF	Tetrahydrofuran
TME	Tumor Microenvironment

USA	United States of America
UV-vis	Ultraviolet-Visible
W	Width

Chapter 1

Introduction

This chapter is based on the publication entitled: "*Overview of the application of inorganic nanomaterials in cancer photothermal therapy*" (2020). Biomaterials science. 8: 2990-3020.

1. Introduction

1.1. Cancer

1.1.1. Cancer epidemiology

Cancer is a major healthcare problem being the second leading cause of death worldwide. According to the American Cancer Society, ≈ 1.8 million new cases of cancer are predicted for 2020, as well as about 0.6 million of cancer-related deaths, just in the United States of America (USA) [1]. In Portugal, according to studies from Direção Geral de Saúde (2017), the cancer incidence has been steadily increasing at an annual rate of 3%. Furthermore, this study also reported that by the year 2035 the cancer incidence and mortality would be close to sixty thousand and thirty thousand cases, respectively [2].

Smoking, alcohol consumption, unhealthy diet, genetic predisposition, and physical inactivity are some of the main cancer risk factors identified worldwide and associated with an increased probability of developing cancer [3]. Smoking is the single most important risk factor for cancer and is responsible for approximately 22% of cancer-related deaths globally. Aging is another key factor in the development of cancer due to the prolonged exposition to carcinogens as well as to the possible accumulation of mutations and errors in the cellular repair mechanisms [4, 5].

1.1.2. Cancer development and hallmarks

Cancer is a family of diseases that can affect any organ of the body [6]. The transformation of a normal cell into a tumor cell is a multi-step process driven by several somatic mutations. Cumulative changes at the cellular, genetic, and epigenetic levels as well as abnormal cell division progressively transform a normal cell into a tumor cell, leading to uncontrolled cellular proliferation, denominated carcinogenesis [7]. Moreover, the concept of cancer evolved from this simple uncontrolled proliferation to a complex and heterogeneous population of cells composed by tumor cells and endogenous stromal cells, denominated as the tumor microenvironment (TME). Different stromal cells were identified in the TME, such as bone marrow, composed of mesenchymal, endothelial, immune, adipocytes, and fibroblasts cells; connective tissue, composed of fibroblasts and mesenchymal cells; adipose tissue, composed of adipocytes; and blood vessels, composed of pericytes and endothelial cells [8-10]. This complex interaction favors the remodeling of the tumor extracellular matrix as well as promotes the migration of cells, the neoangiogenesis, the cell invasion, the drug resistance, and the tumors cells' evasion from the immunosurveillance by stimulating the production of different growth factors, chemokines, and cytokines [11, 12]. In fact, the interaction of cancer cells with the constituents of the TME can trigger dynamic signaling circuits that

promote cancer maintenance and progression. Hanahan and Weinberg attempted to organize the dense complexity of cancer biology into ten hallmarks: self-sufficiency in growth signals, insensitivity to anti-growth signals, evading apoptosis, limitless replicative potential, sustained angiogenesis, tissue invasion, and metastasis, reprogramming energy metabolism, evading immune response genome instability and mutation, and tumor-promoting inflammation [13].

One of the most important characteristics of cancer cells is their ability to preserve growth pathways and proliferative signaling. Cancer cells are able to sustain a proliferative state by producing high levels of growth signals, acting in autocrine or paracrine signaling, to promote tumor progression. Otherwise, growth inhibitory pathways are often downregulated to allow the tumor's escape from this suppressing signals [14, 15]. Even in the presence of growth signaling, the strict regulation of the cell cycle via regulatory proteins keeps the cell proliferation under control. In cancer cells, the cell cycle is deregulated and the checkpoint inhibitors are disrupted [16]. The retinoblastoma protein and the p53 are two key regulators of the cell proliferation and are frequently mutated in cancer cells (*e.g.* p53 mutations were detected in 50% of sequenced tumors), which allows their evasion from the programmed cell death [17].

Another hallmark of cancer cells is the overexpression of telomerase. This enzyme is capable of reconstituting the telomeric ends of chromosomes, maintaining sufficient length for further replication. Therefore, the overexpression of telomerase maintains telomeres integrity during the successive replicative cycles of cancer cells, which prevents DNA damage/cell death and renders to them an unlimited cell proliferation capacity [18]. Additionally, the formation of new vasculature is essential for the tumors to grow beyond 2-3 mm^3 or metastasize [19]. In this way, the cancer cells can induce changes in the angiogenic machinery to facilitate access to oxygen and nutrients [20]. The hypoxia arises as one of the most important triggers for angiogenesis in cancer tissues [21]. Endothelial cells possess several oxygen-sensing mechanisms, mainly those interfacing with the hypoxia-inducible transcription factor family, regulating the expression of a multitude of genes not only involved in angiogenesis, but in cell survival, metabolism, and inflammation as well [22]. Other factors that can induce tumor angiogenesis include the metabolic rewiring of endothelial cells creating an acidic TME, changes in genes that control the production of angiogenic regulators, mechanical stress, and infiltration of the inflammatory cells (*e.g.* expression of vascular endothelial growth factor-A (VEGF-A), angiopoietins, and platelet-derived growth factors) [23, 24].

More recently, it was also proposed that cancer cells can prevent its recognition and destruction by the immune system and reprogram their metabolism (*e.g.* adjustments in glycolytic pathways) to improve tumor proliferation and progression [20]. Additionally, the presence of inflammatory cells in the TME can also impact on tumor development. In fact, research data indicates that the tumor-associated inflammatory process might fortify the cancer cells stimulating them to survive and progress. Further, several studies have been linking the chronic inflammation to cancer occurrence, where inflammatory cells can provide growth factors to malignant cells (*e.g.* TGF-β family) and facilitate the development of other hallmarks through the expression of cytokines (*e.g.* TNF and JNK) and proteases (*e.g.* MPP-2). Moreover, the inflammatory cells can produce chemical substances that can cause genetic mutations in the TME [25]. As a result, all these factors can aid malignant cells to proliferate and survive or even to metastasize [26]. Another hallmark of cancer is the deregulation of cellular energetics. Cancer cells mainly depend on anaerobic glycolysis, which produces less energy, to adjust their high energy requirements (*i.e.* increased cell growth and replications). Nevertheless, to compensate for the anaerobic glycolysis, cancer cells upregulate glucose transporters, mainly Glut-1, increasing glucose influx to the cytoplasm. Further, cancer cells present an increased expression of most of the glycolytic enzymes (*e.g.* hexokinase II (HKII), pyruvate dehydrogenase kinase (PDK), and PKM2). Otherwise, the glycolysis can also be induced in cancer cells by activated oncogenes, such as RAS, Myc, and HIF-1afa, and mutated P53 [27].

1.1.3. Conventional treatments

The conventional therapies (*e.g.* surgery, chemotherapy, and radiotherapy) currently used in the clinic present several drawbacks, such as low solubility and selectivity, that hinder their therapeutic effectiveness [28]. This reality has been pushing the researchers to develop new and more effective therapeutic approaches, such as immunotherapy, gene therapy, and hyperthermia [29-31].

Hyperthermia-based cancer treatments explore the exposition of the target tissue to high temperatures that can induce the death of cancer cells (*i.e.* thermal ablation, induced by temperatures superior to 45 °C) or increase the cancer cells sensitivity to other therapeutic modalities (mild hyperthermia, temperatures between 40 and 45 °C) [32]. In conventional hyperthermia, the temperature increase in the target tissue is often achieved through outside-in approaches (*e.g.* superficial hyperthermia, regional hyperthermia, and whole-body hyperthermia based on the utilization of thermal bath, microwaves, and radiofrequency) [33]. Such creates a temperature gradient that peaks in the body surface and decreases with the distance from the external heat source [34].

Therefore, the healthy tissues will also be affected by the temperature increase leading to undesired side-effects [35].

With this in mind, researchers have been focused on the development of more efficient hyperthermia approaches, particularly those capable of inducing a localized (*i.e.* tumor confined) temperature increase [36]. In this field, nanoparticles capable of generating heat in response to outside stimuli have been used to surpass the limitations of conventional hyperthermia approaches (Figure 1) [37]. In fact, the size of the nanoparticles confers to them the innate capacity to become accumulated on the tumor by taking advantage of the defective vasculature in this tissue (the enhanced permeability and retention (EPR) effect and/or the vascular bursts) [38]. Then, the nanoparticles can mediate the localized thermal destruction of the cancer cells triggered by external stimuli, minimizing the damages on the surrounding healthy tissues [39]. Such features allowed the development of several nanomedicine-based hyperthermia approaches that can be classified according to the external trigger used for the nanoparticles' activation such as photothermal, magnetic hyperthermia and ultrasound hyperthermia therapies [40-42].

Among them, the nanomaterials' mediated photothermal therapy promotes the selective death of cancer cells by irradiating the target area with laser light [43]. In the literature, several materials have already been explored to mediate this effect, such as gold, carbon, copper, tungsten, iron, and molybdenum [44-49]. Moreover, in this approach, it is essential the utilization of the NIR radiation, particularly the NIR-I and NIR-II radiation, since the major biological components (*e.g.* proteins, melanin, hemoglobin, collagen, and water) present minimal or insignificant absorption in this region of the spectra [50, 51]. In this way, the utilization of radiation in the 750-1200 nm region guarantees the reduction of the off-target interactions and the maximum penetration in the human body, enhancing the therapeutic outcome [43].

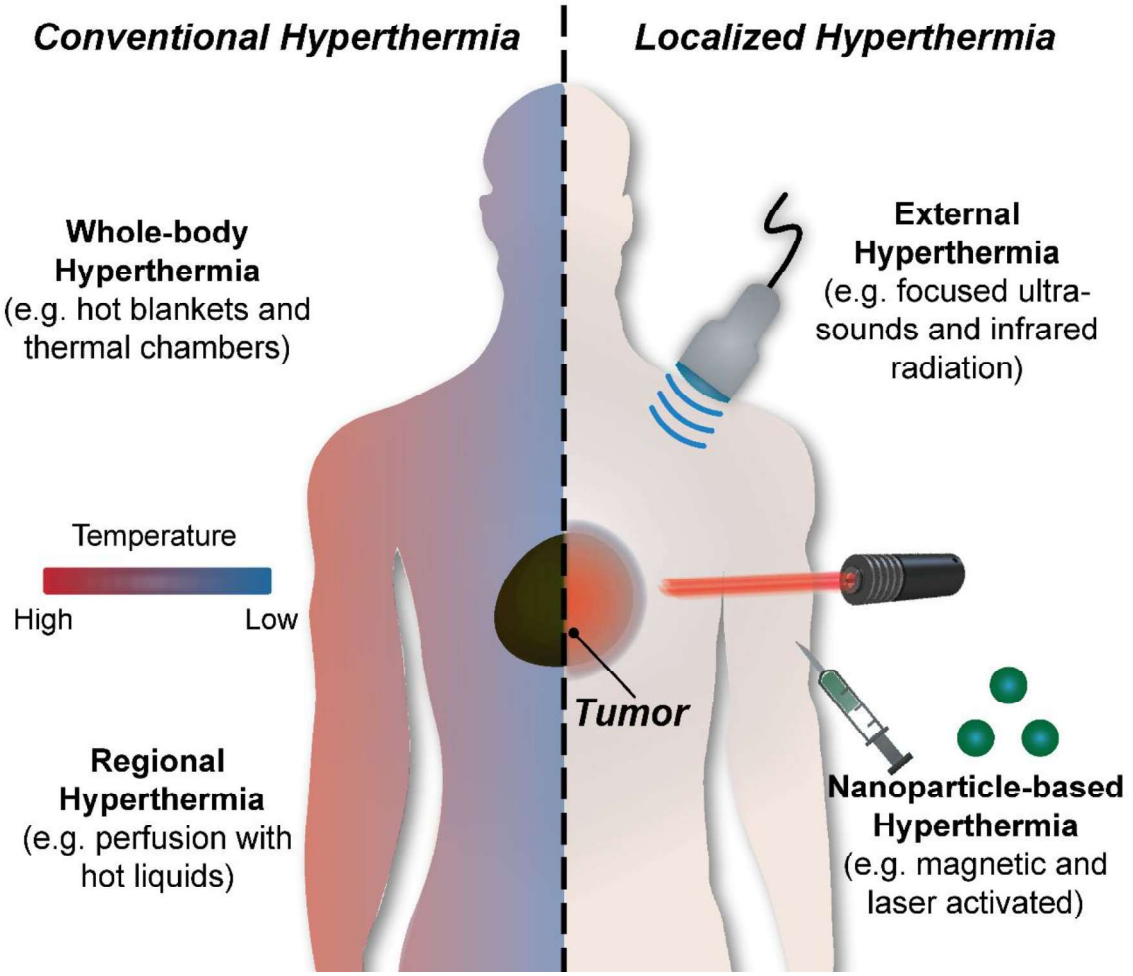

Figure 1: Representation of conventional and localized hyperthermia. Conventional hyperthermia creates a heat gradient from the surface region of the body to the interior. The localized hyperthermia approaches promote the specific heating of the tumor tissue, avoiding damages in the surrounding areas.

1.2. Nanoparticle-mediated photothermal therapy

1.2.1. General properties

The nanomaterials cancer photothermal therapy (PTT) involves the irradiation of a specific area with a NIR laser that leads to the activation of the nanostructures accumulated within the tumor [52]. Then, the local conversion of the NIR laser energy into heat mediated by nanoparticles induces a localized hyperthermia effect [53]. Therefore, the nanomaterials' tumor selectivity is essential for PTT effectiveness [54]. Nanoparticles' accumulation in the tumor tissue can occur through passive or active targeting phenomena [55]. The passive targeting arises due to the high proliferative rate of cancer cells, leading to the formation of defective vascular, capillaries with fenestration sizes superior to 200 nm, and lymphatic vessels [56]. This abnormal vasculature facilitates the nanoparticles' extravasation and retention in the tumor tissue [57]. Furthermore, more recently, it was also described that the enhanced permeability in tumors can be the result of transient vascular bursts that allow the diffusion of the

blood to the tumor interstitium [58]. On active targeting, the accumulation of the nanoparticles on the tumor can be mediated by receptor-ligand or antigen-antibody interactions, that favor the nanoparticles interact with the cancer cells [59]. Usually, in the active targeting, the nanomaterials are modified to explore the specific recognition of molecules overexpressed at the tumor site, such as the folate and biotin receptors [60, 61].

Nevertheless, independently of the process that mediates the accumulation of the nanoparticles in the tumor tissue, prolonged blood circulation will increase the nanoparticle's probability to accumulate/interact with the cancer cells [62]. In this way, there are several physicochemical parameters (*e.g.* nanoparticle size, surface charge, and corona) that impact the nano-bio interaction and consequently on the blood circulation time (reviewed in detail by [63-65]). For example, the development of nanoparticles with sizes from 100 to 200 nm has been described as optimal for the intravenous administration in the human body [38]. This size range avoids the rapid clearance by the kidneys (nanoparticle size <5 nm), the accumulation in the liver (nanoparticle size <50 nm) and spleen (nanoparticle size >200 nm) while maintaining the capacity to extravasate through the tumor fenestrae (nanoparticle size <200 nm) [57]. Despite this ideal size values, Li and co-workers demonstrated that by increasing the size of gold nanoparticles (6.2, 24.3, 42.5, and 61.2 nm) a higher nanoparticle uptake by liver and spleen (44-55 %ID/g and 30-40 %ID/g, respectively) occurred after 24 h of administration [66]. Similarly, Larsen and co-workers also observed an ≈ 8-fold increase in the PEGylated iron oxide nanoparticles uptake by macrophage cells by increasing the size from 20 to 40 nm [67]. Moreover, Liu *et al.* reported that PEGylated gold nanoparticles with 30 nm of size present an increased tumor uptake when compared to their counterparts with 60 nm (2.11 ± 0.64 vs. 0.88 ± 0.46 %ID/g) [68]. Additionally, Perrault and colleagues observed that PEGylated gold nanoparticles with 20 nm presented an enhanced diffusion in the tumor interstitial space when compared to other equivalents with higher size, 60 and 100 nm [69].

On the other hand, the nanoparticle surface charge can favor the uptake by the reticuloendothelial system (surface charge <-10 mV) and the interaction with serum proteins (surface charge >10 mV) [70]. Therefore, nanoparticles with a neutral surface charge (±10 mV) often present the longest circulation time [71]. Additionally, the adsorption of proteins on the surface of the nanoparticle can induce changes on the surface charge, prompt the particle aggregation, or even facilitate the nanoparticles' recognition by the reticuloendothelial system [72]. Such can be overcome by the introduction of hydrophilic and antifouling materials (*e.g.* polyethylene glycol (PEG) and

polyoxazolines) or even self-membranes on the nanoparticle surface (Figure 2) [73]. Sharker and colleagues demonstrated that the functionalization of tungsten oxide nanoparticles with hyaluronic acid increased their biocompatibility even at high doses (1 mg/mL) [74]. Xuan and coworkers reported that the gold nanoshells coating with self-macrophage membranes improved the blood circulation time and tumor accumulation from ≈ 1.6 to ≈ 7.5% ID/g [75].

Nonetheless, when the nanomaterials are aimed for cancer PTT applications, the initial focus of the researchers is the nanoparticle light/heat conversion efficiency. In nano-sized photothermal agents, the photothermal capacity is closely related to the surface plasmon resonance (SPR) that corresponds to the light-induced resonant oscillation of the free electrons on the particle's surface [76]. In this process, the nanomaterials can mediate light scattering or absorption [77]. The light absorption induces the excitation of the free electrons on the particle's surface and the subsequent electrons' relaxation can release the absorbed energy in the form of luminescence or heat [78]. In PTT, nanoparticles with high absorption efficiency and low luminescent capacity are required to guarantee the most effective light/heat conversion. Additionally, a localized temperature increase will only occur when the laser irradiation time is superior to the nanoparticle relaxation time since for shorter irradiation times the generated heat is only confined to the nanoparticle and does not diffuse to the external medium [35]. Therefore, both the nanoparticle light/heat conversion efficiency and laser parameters (*e.g.* irradiation time and power) have to be optimized for an efficient PTT be accomplished (reviewed in detail by [37, 79, 80]). Nevertheless, it is worth noticing that the NIR light can only penetrate a few centimeters in the human body, which will hinder the biological performance of the PTT mediated by nanomaterials in deep-seated tumors [47, 76]. Therefore, researchers have developed different approaches to enhance the nanomaterials' antitumoral performance, such as the application of tissue implanted NIR light sources or even by combining the PTT with chemotherapy, immunotherapy, and photodynamic therapy [81-84].

In the following sections, the application of gold-based nanomaterials for mediating a tumor-localized photothermal effect (Table 1) is described as well as their combination with other therapeutic approaches, highlighting the nanoparticle physicochemical parameters that influence the PTT effectiveness.

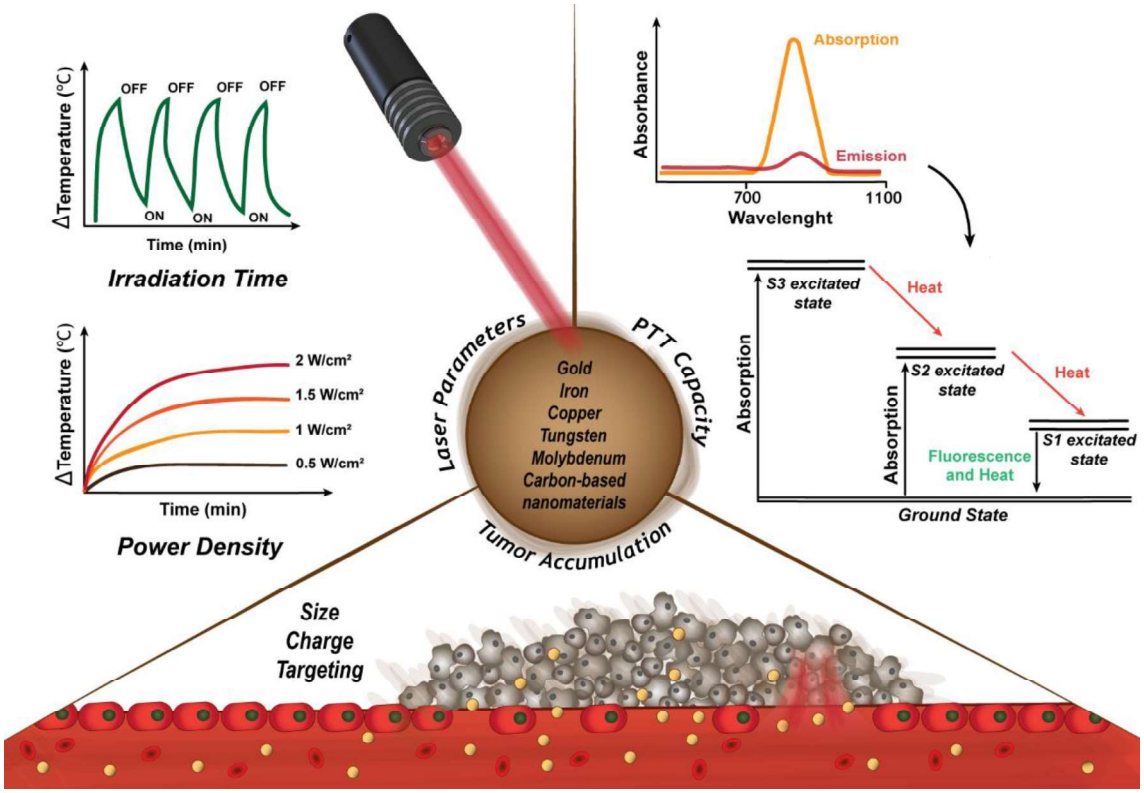

Figure 2: Representation of the main factors that affect the PTT mediated by nanomaterials. The thermal effect induced by nanoparticles is directly impacted their photothermal conversion efficiency (*i.e.* capacity to convert the energy absorbed into heat) and the irradiation parameters, such as the irradiation time and the power density. Further, the nanomaterials accumulation in the tumor tissue will affect therapeutic effectiveness.

1.3. Gold nanomaterials

The gold nanostructures are one of the most explored nanomaterials to mediate a photothermal effect, as already reviewed in detail in [80, 85, 86]. Such is attributed to the localized SPR of gold nanomaterials that can mediate a strong light absorption and/or scattering [87]. These nanostructures are usually produced by promoting the gold nucleation upon the reduction of gold salts, using stabilizing agents to avoid nanoparticle aggregation [88, 89]. Further, the optimization of the synthesis process allows the tuning of the resonance wavelength to the NIR region of the spectra endowing a strong PTT capacity to the gold nanomaterials [90]. Several works already demonstrated that the gold nanomaterials PTT capacity is dependent on the particle size, shape (*e.g.* spheres, nanorods, nanostars, and nanocages), and organization [80, 91, 92].

1.3.1. Gold nanosphere-based structures

The gold nanospheres present a typical absorption band in the 500 to 550 nm region that can suffer a redshift, by increasing the particle size [93]. Nevertheless, the gold nanosphere size increase does not allow the fine-tuning of the absorption peak to the NIR region (*i.e.* usually only up to 600 nm) [94, 95]. When PTT applications are

envisioned, the application of gold nanospheres occurs when organized in nanosphere shells and/or clusters. The localized SPR of gold nanosphere-based shells and clusters presents a shift in the absorption peak from the visible to the NIR region of the spectra when interparticle gaps are decreased [96-98]. Such is attributed to the interparticle interactions that result in the coupling of the plasmon oscillations due to interactions of the near-field of one particle with the adjacent ones in close proximity [99, 100]. Li *et al.* produced U11 targeted gold nanoclusters containing a cathepsin E sensitive PDT therapy prodrug (5-ALA) and a cyanine dye (Cy5.5) for the pancreatic ductal adenocarcinoma photothermal and photodynamic therapy [101]. For that purpose, gold spheres with 10 nm in diameter were initially modified with Cys-Arg-Gln-Ala-Gly-Phe-Ser-Leu-5-ALA (CRQAGFSL-5-ALA) and Cys-Arg-Gln-Ala-Gly-Phe-Ser-Leu-Cy5.5 (CRQAGFSL-Cy5.5). Then, the gold nanoparticles were crosslinked using 1,9-nonanedithiol (*i.e.* exploring) gold-thiol interactions to form spherical gold clusters with ≈ 53 nm in diameter, which were further functionalized with PEGylated U11 targeting peptides. The resulting gold nanoclusters presented a redshift on the gold spheres absorption peak from the 532 nm to 544 nm, as well as an increased absorption capacity in the 700-800 nm region. Additionally, the authors reported that the gold nanoclusters could mediate a temperature increase from 20 °C to around 50 °C after being irradiated with a NIR laser (750 nm, 2 $W.cm^{-2}$ for 5 min). Moreover, the U11 targeted gold nanoclusters revealed to be biocompatible at concentrations as high as 5 nM (*i.e.* PANC1 CTSE cells viability was superior to 80% after 24 h of incubation with gold nanoclusters) and showed a preferential accumulation on the tumor tissues. These authors also demonstrated that the intravenous administration of U11 targeted gold nanoclusters containing 5-ALA and Cy5.5 (2 pmol per mouse) could mediate an antimoral effect. In fact, an inhibition of the tumor growth was reported when only PDT or PTT treatments were performed, whereas the combinatorial PDT/PTT treatment resulted in the almost complete eradication of the tumors, after 15 days. In a similar approach, Park and colleagues produced albumin nanoparticles containing gold nanoclusters and Cy5.5 for the cancer fluorescence imaging and PTT [102]. The particles were produced by mixing the gold nanospheres (≈ 4.4 nm in diameter) with different amounts of albumin to promote their agglomeration. A close entrapment of the gold nanospheres on the albumin particles resulted in a greater absorbance over the 600–900 nm region. Moreover, nanoparticles formulated with 10 mg/mL of albumin were able to mediate an increase in the temperature up to 70 °C after irradiation with a NIR laser (808 nm, 1.5 $W.cm^{-2}$ for 10 min). Additionally, the *in vivo* assays demonstrated that the intravenous administration of albumin/gold nanoclusters (200 μL at 10 mg/mL) remarkably suppressed the tumor growth. A reduction of the tumor size from 150 mm^3 to 17.8 mm^3 upon NIR laser irradiation (808 nm, 1.5 $W.cm^{-2}$

for 10 min) was noticed. Wang and coworkers developed gold nanoshells coated chitosan modified liposomes loaded with resveratrol for the chemo-PTT of cancer [103]. For that purpose, small-sized gold spheres were attached to the surface of chitosan modified liposomes (formation of Au-N bond) and subsequently reacted with a growth solution (gold precursor and reducing agent). The growth solution allows the assemble of new gold atoms on the surface of the small-sized gold spheres forming large gold nanoparticles and a uniform shell at the liposome surface. The authors reported a redshift in the absorption peak with the growth of the gold nanoparticles in the surface of liposomes, exhibiting a broad absorption band in the 550-800 nm region. Additionally, the authors also observed that the photothermal effect generated by these nanomaterials remained constant during 5 cycles of irradiation with a NIR laser (808 nm, 2 $W.cm^{-2}$ for 5 min), reaching the maximum temperature of 66.7 °C. Further, a temperature-responsive drug release from the gold shell coated liposomes was observed. In fact, the resveratrol release was increased upon irradiation with a NIR laser due to the phase change of the liposomes. In the *in vitro* studies, the photothermal effect mediated by the gold nanoshell coated chitosan modified liposomes (54 μg/mL) induce a reduction of the HeLa cells viability up to 57.3%. This cytotoxic effect was further enhanced when the heat generated by these nanomaterials was combined with the resveratrol action, leading to cell viability values inferior to 20%. Similarly, Manivasagan *et al.* developed an anti-EGFR paclitaxel loaded-thiol chitosan-layered gold nanoshells for the fluorescence/photoacoustic imaging and chemo-PTT of cancer (Figure 3). [104]. In this approach, gold nanoshells composed of gold spheres with 9 nm in diameter were created on the surface of silica cores (120 nm). Then, the surface of this material was functionalized with thiolated chitosan through gold-thiol interactions and further conjugated with anti-EGFR antibody. The resulting nanoparticles presented a strong absorption band in the 700-1200 nm region with a peak of absorption at 799 nm. Such resulted in the heat generation upon the irradiation of the chitosan-layered gold nanoshells with a NIR laser (808, 1.2 $W.cm^{-2}$ for 5 min), reaching 52.7 °C when a nanoparticle concentration of 175 μg/mL was used. Additionally, these authors also observed that the heat generated could be used to trigger the paclitaxel release from the chitosan layer present on the surface of the gold nanoshells, in fact after 48 h, at pH 5, the group subjected to 5 irradiation cycles released 91.09% of the drug, contrasting with the 53.83% recorded for the non-irradiated group. The *in vivo* assays demonstrated that the tumor irradiation with a NIR laser (808, 1.2 $W.cm^{-2}$ for 5 min) 5 h after the intravenous administration of the anti-EGFR paclitaxel loaded-thiol chitosan-layered gold nanoshells (175 μg/mL) provoked an increase in the tumor temperature, reaching a maximum of 61.9 °C. Further, the authors also observed that the

combinatorial action of the paclitaxel and PTT resulted in the eradication of the tumors (97.43% tumor inhibition rate).

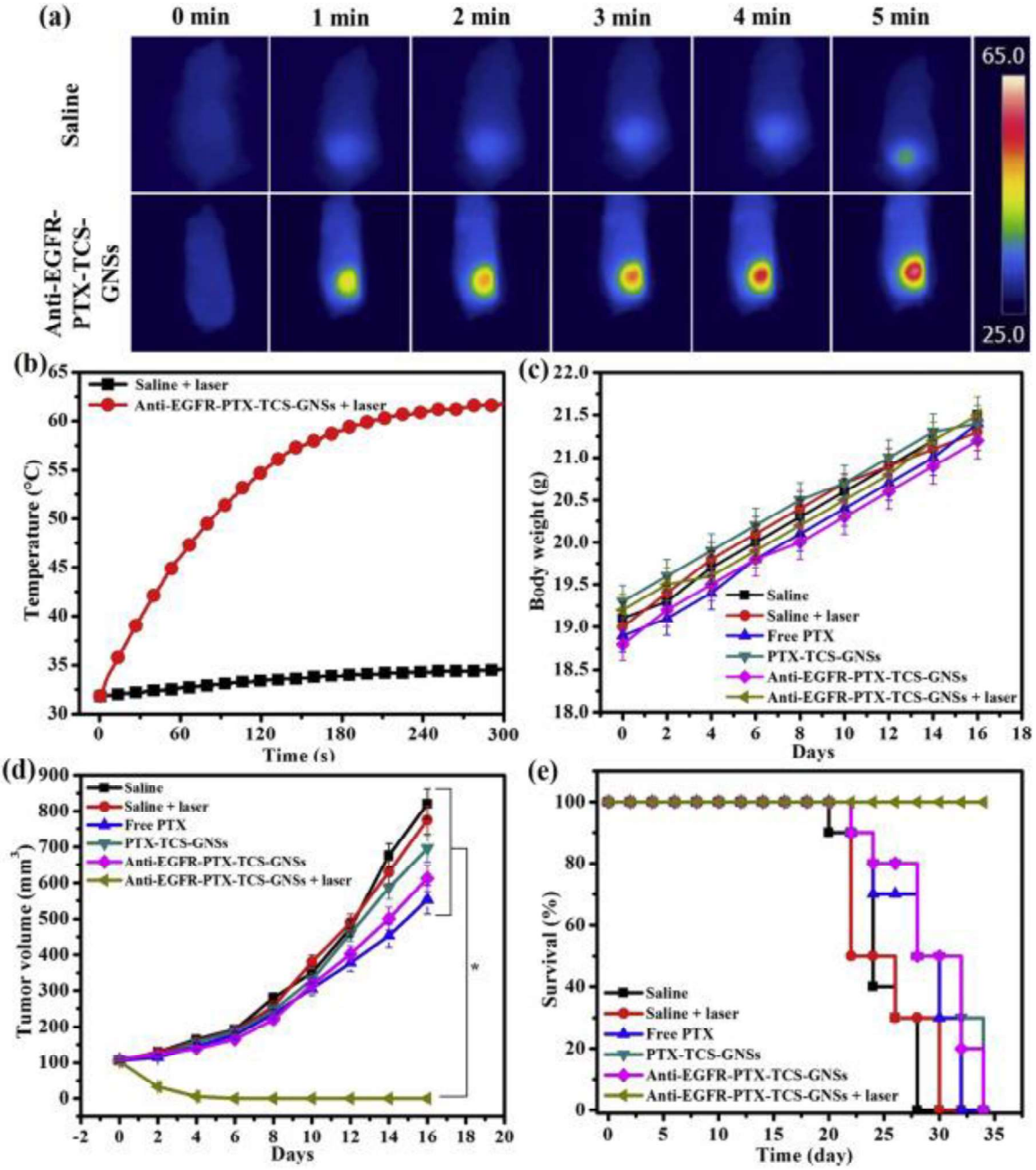

Figure 3: Evaluation of the antitumoral capacity of anti-EGFR-PTX-TCS gold nanoshells. Thermal images (A) and temperature variation curves (B) of tumors after irradiation with NIR laser (808 nm, 1.2 W.cm^{-2}). Analysis of the mice's body weight changes (C), tumor volume evolution (D), and mice survival (E) after different treatments (adapted from [104]).

1.3.2. Gold nanorods

The gold nanorods have been one of the most explored morphologies to develop gold nanostructures for photothermal applications [105]. The gold nanorods present two absorption bands, a weaker one in the visible region of the spectrum (*i.e.* transverse

resonance, surface electron oscillation along the nanorods width) and a more intense band that can be fine-tuned to the NIR region (*i.e.* longitudinal resonance, surface electron oscillation along the length of the nanorods) [47, 106]. The absorption band corresponding to the longitudinal resonance is dependent on the nanorod aspect ratio (*i.e.* rod length/width coefficient), being nanorods with aspect ratios between 3 and 6.6 applicable in PTT [107]. Mackey and colleagues studied the photothermal potential of nanorods with different dimensions (Length × Width: 38 × 11, 28 × 8, and 17 × 5 nm) [108]. The obtained results demonstrated that despite the similar aspect ratio (3.4-3.5), the different gold nanorods presented the longitudinal absorption peaks at 740, 770 and 755 nm for the 38 × 11, 28 × 8, and 17 × 5 nm nanorods, respectively. This difference resulted in an increased heat conversion capacity for the 28 × 8 nanorods after irradiation with a NIR laser (808 nm and 5.8 $W.cm^{-2}$) for 2 min, the photothermal heat conversion factor was 2.05 and 1.40 times superior to that recorded for the 38 × 11 and 17 × 5 nm nanorods. Moreover, the authors also reported increased cytotoxicity towards HSC-3 cells (oral squamous cell carcinoma) based on the photothermal effect of the 28 × 8 nm gold nanorods, cell viability of ≈ 100, ≈ 17, and ≈29% for nanorods with dimensions of 38 × 11, 28 × 8, and 17 × 5 nm. Zhang and coworkers developed a PEG-biotin functionalized DNA conjugated gold nanorods for the targeted chemo-PTT of breast cancer [109]. The produced gold nanorods presented an aspect ratio of 3.5 with a length × width of 50 × 14 nm. The authors modified the surface of the nanorods by using thiolated-PEG modified with biotin and thiolated-DNA enriched with doxorubicin (DOX) for promoting the establishment of gold-thiol interactions. The produced nanomaterials presented the characteristic absorption peaks of gold nanorods at 512 nm (transversal surface plasmonic resonance) and 806 nm (longitudinal surface plasmonic resonance), which could be exploited to mediate a strong photothermal effect reaching the ≈ 45 °C after irradiation with a NIR laser (808 nm, 5 $W.cm^{-2}$ for 30 min, gold nanorods at 5.82 μg/mL). On the other hand, the gold nanorods presented a pH and NIR responsive drug release due to the DOX intercalation with the DNA grafted on the particles surface, ≈ 60% drug was released when irradiated with a NIR laser (808 nm, 5 $W.cm^{-2}$ for 30 min) and ≈ 50% after being incubated at pH 5.0. In the *in vitro* assays, the authors observed that the combinatorial treatment mediated by the gold nanorods (gold nanorods at 5.82 μg/mL and DOX 2 μM, NIR laser 808 nm, 5 $W.cm^{-2}$ for 30 min) inhibited the MCF-7/ADR cells cell growth in 81%.

1.3.3. Gold nanostars

The gold nanostars absorption band is dependent on the core size and tips length, width, and number [110]. In general, an increase in the gold nanostars core size, tip length as well as sharper tips promote a shift in the absorption peak to the NIR region [111]. Espinosa *et al* produced gold nanostars with 25, 55, 85, 120, and 150 nm in diameter and observed that the samples with 25 nm presented two absorption peaks at 550 and 700 nm, whereas the samples with 55, 85, 120, and 150 nm in diameter presented a single absorption band at 790, 800, 900, and 950 nm, respectively [112]. Further, the authors also reported that upon irradiation with NIR laser (808 nm, 1 $W.cm^{-2}$) for 10 min, the nanostars with a diameter of 25, 85, and 150 nm mediated an increase in temperature of ≈ 18 °C, ≈ 45 °C, and ≈ 36 °C. Xia and colleagues developed IR-780 iodine-loaded gold nanostars functionalized with matrix metalloproteinases (MMP2) polypeptides (Ac-GPLGIAGQ) and bovine serum albumin (BSA) for the lung cancer imaging and photothermal/photodynamic therapy [113]. For that purpose, the gold nanostars were conjugated with BSA via gold thiol interactions. Then, MMP2 polypeptides were grafted on nanostars' surface through carbodiimide chemistry and loaded with the IR-780 molecules. The resulting nanoparticles presented a mean diameter of 80 nm and a strong absorption band in the 700-800 nm region. The data obtained revealed that the gold nanostars (20 μg/mL) irradiation with a NIR laser (808 nm, 0.8 $W.cm^{-2}$ for 5 min) could mediate a temperature increase up to 63 °C. In the *in vivo* studies, the intravenous administration of the IR-780 iodine-loaded gold nanostars functionalized MMP2 and BSA (IR-780, 1 $mg.kg^{-1}$) mediated an increase on the tumor temperature up to 46 °C (808 nm, 0.8 $W.cm^{-2}$ for 5 min), which combined with the IR-780 action led to a 93% reduction of the tumor volume.

1.3.4. Gold nanocages

Gold nanocages, nanostructures where the gold is only present at the particle surface, present an absorbance band that can be tuned to the NIR region by optimizing the wall thickness [114]. In fact, the increase in the amount of gold source during the synthesis procedure is linked to a redshift in the absorption peak [115]. Huang and coworkers developed polyethyleneimine (PEI)-modified and folate receptor-targeted PEGylated gold nanocages enriched with microRNA-181b inhibitor aimed for the cancer gene and PTT [116]. The gold cages presented 50 nm in size, a hollow structure, and pores with 5 nm. Then, thiol-PEG-folic acid (FA) chains were attached on the particle surface via gold-thiol interactions, and the PEI was conjugated using lipoic acid as a linker. The resulting nanoparticles presented the absorption peak at 802 nm and upon irradiation with a NIR laser (808 nm, 1.25 $W.cm^{-2}$ for 10 min) induced the temperature increase up to ≈ 55 °C,

when a concentration of 9.7 μg/mL was used. In the *in vivo* studies, the intravenous administration of gold nanocages (gold content at 8.5 $mg.kg^{-1}$) result in an increase in the temperature up to 53.6 °C, which combined with the action of the anti-microRNA-181b inhibited the liver tumors progression and increased the mice median survival times from 36 to 60 days. In turn, Sun and colleagues developed DOX-loaded gold nanocages coated with 4T1 cancer cell membranes for the chemo/PTT of breast cancer [117]. For that purpose, DOX-loaded gold nanoshells with 70.5 nm of diameter were extruded with 4T1 cell membrane vesicles through a 100 nm polycarbonate membrane. The resulting nanomaterials presented the absorption peak at 760 nm and could mediate a temperature increase of ≈25 °C upon irradiation with NIR laser (808 nm, 2.5 $W.cm^{-2}$ for 8 min). Moreover, in the *in vivo* studies, the combinatorial treatment (intravenous administration 91 $mg.kg^{-1}$ of gold nanoshells) suppressed the tumor progression and decreased the number of lung metastases by 98.5%.

1.4. Clinical trials

Currently, a wide number of nanomedicines have been approved for cancer treatment, mainly those exploring cancer chemotherapy [118]. Nevertheless, despite the promising properties and therapeutic potential demonstrated by the approaches based on hyperthermia mediated by nanomaterials, their translation into the clinic is still limited. In fact, most of the approaches exploring the nanomaterials-mediated hyperthermia under clinical development are based on the utilization of the magnetic fields for promoting the heat generation [119].

Among them, NanoTherm® (MagForce AG) is applied in the treatment of glioblastomas and consists of an aqueous suspension of FeO nanoparticles, that produces heat in the presence of alternating magnetic fields [120, 121]. The nanoparticles possess an average size from 10-15 nm and are injected into the tumor or in the cavity wall during the tumor resection. The FeO core (≈ 111 mg/mL Fe concentration) are coated with amino silanes to ensure that the nanoparticles remain stable in the tumor tissue. After reaching the tumor site, the iron oxide nanoparticles are activated by an external alternating magnetic field, for six one-hour sessions (magnetic hyperthermia). Thus, the tumor thermal ablation is performed, usually, at temperatures ≈ 44-45 ºC, which can also sensitize the cells to other therapeutic approaches such as chemotherapy or radiotherapy [119, 122]. The efficacy of Nanotherm® presents improvements when combinate with other therapies [123, 124]. This approach was approved by the European Medicines Agency for the treatment of brain tumors and is currently under clinical investigation in the USA [119].

The Magnablate I is another iron oxide nanoparticle-based magnetic treatment under clinical trials for the treatment of prostate cancer [125]. A clinical phase of the study (ClinicalTrials.gov Identifier: NCT02033447, data still not available) has been developed to test where the nanoparticles are located after the intratumoral injection and if any prostate-related side effects or irreversible damages can occur.

Otherwise, Aurolase® (Nanospectra) remains has a unique nanoparticle under clinical evaluation for the PTT of cancer [126]. Two clinical trials are currently being performed using this technology, a study to evaluate the efficacy of the Aurolase® therapeutic approach in primary and/or metastatic lung tumors (ClinicalTrials.gov Identifier: NCT01679470) and the determination of the antitumoral capacity in patients with refractory and/or recurrent tumors of the head and neck (ClinicalTrials.gov Identifier: NCT00848042).

This technology designated by Aurolase® uses PEGylated gold nanoshells with approximately 150 nm of the diameter that possesses a high absorption peak in the 800 nm, which allows their application in PTT. When the nanoparticles are intravenously injected, they explore the EPR effect to passively accumulate in the tumor site. The posterior NIR laser radiation may result in the cellular death and tumor regression [122, 127]. In the first clinical trial (ClinicalTrials.gov Identifier: NCT01679470), a single dose of gold nanoparticles was administered in patients with primary and/or metastatic tumors of the lung (with airway obstruction). Then, the PTT effect was triggered via bronchoscopy using an optical fiber emitting NIR light (testing the irradiation of an escalating dose) [127, 128]. In the second PTT Aurolase® clinical study, patients with acute and/or chronic neck and head tumors received a single dose of gold nanoparticles through intravenous administration and were subjected to one or multiple doses of laser irradiation (808nm). Three treatment groups (5 patients each, testing variation in the laser's power density) performed the study and were monitored during 6 months after treatment. Both clinical trials were already completed in 2014, but results have not yet been published (ClinicalTrials.gov Identifier: NCT00848042) [127, 128].

Table 1: Overview of the properties of gold nanoparticles for application in PTT. (W) Width; (L) Length; (AR) Aspect ratio; (MS) Mesoporous silica; (D) Diameter.

Material	Morphology and surface modification	General properties	Absorption band	Dose	PTT			Type of cancer *in vitro* / *in vivo*	Ref.
					Laser	Temperature	PTT conversion efficiency		
Gold	Rabies virus-mimetic silica-coated gold nanorods	L: 79.9 nm; W: 20.1nm; AR: 4 Silica shell: 13.8 nm	820 nm	0.1 mM	808 nm, 1.5 $W.cm^{-2}$ for 5 min	$T_{max} \approx$ 50.0 °C	-	N2a cells / N2a tumor-bearing mice	[129]
	HA and RGD with MS-coated gold nanorod	L:50 nm; W:10 nm; Silica shell: 15 nm	520 and 780 nm	40 μg/mL	808 nm; 2.0 $W.cm^{-2}$ for 4 min	T_{max}= 43.5 °C	-	SKOV-3 cells	[130]
	MS-coated gold nanorod loaded with Indocyanine green, end-capped with β-cyclodextrin and RLA peptide anchored	L: 57.3 nm; W: 16.2 nm; AR: 3.47; Silica shell: 21 nm	813 nm	4.2 mg/mL	808 nm; 2.0 $W.cm^{-2}$ for 9 min	ΔT= 31.2 °C	-	MCF-7 cells / MCF-7 tumor-bearing mice	[131]
	MS-coated gold nanorods coated with *in situ* formed silver nanoparticles	L: 46 nm; W: 19 nm; Silica shell: 15 nm	684 nm	100 μg/mL	780 nm; 3.0 $W.cm^{-2}$ for 10 min	T_{max}= 44.6 °C	-	HeLa and L02 cells	[132]

	Mesoporous silica-coated gold nanorods, β-cyclodextrin as gatekeeper functionalized with lactobionic acid and PEG	L: 39.8 nm; W: 10.2 nm; AR: ≈ 3.9; Silica shell: ≈ 14 nm	677 and 791 nm	25 and 50 μg/mL	808 nm; 0.37 and 1.01 $W.cm^{-2}$ for 8 min	T_{max}≈ 64.8 °C (50 μg/mL and 1.01 $W.cm^{-2}$) T_{max}≈ 39.1 °C (25 μg/mL and 0.37 $W.cm^{-2}$)	-	HepG2 and COS7 cells / HepG2 tumor-bearing mice	[133]
	MS coated gold nanorods capped with Poly (NIPAAm-co-BVIm)	L: 45 nm; W: 10 nm; AR: 4.5; Silica shell: ≈ 30 nm	850 nm	60 μg/mL	850 nm; 100.0 mW for 5 min	T_{max}≈ 65.0 °C	-	HeLa cells	[134]
	Bacteria-like mesoporous silica coated gold nanorods functionalized with PEG	L: 104.6 nm; W: 68.6nm; AR: 3.7; Silica shell: 23.5 nm	805 nm	0.5 mg/mL	808 nm; 0.25 $W.cm^{-2}$ for 10 min	T_{max}= 45.0 °C	29.6%	4T1 cells / 4T1 tumor-bearing mice	[135]
	Nanostars	Size: 30 nm containing 95.5% gold and 4.5% silver; Size: 60 nm containing 96.9% gold and 3.1% silver	706 nm (60 nm) and 945 nm (30 nm)	0.5 nM (30 nm)	980 nm; 0.8 $W.cm^{-2}$ for 20 min	T_{max}≈ 42.0 °C (30 nm)	94% (30 nm) and 90% (60 nm)	Mouse sarcoma tumor-bearing mice	[68]

	Gold nanostar coated Hollow MS encapsulated with PFH and functionalized with PEG	Nanostar Size: 60 nm; Hollow MS: 200 nm	520 and 795 nm	20 mM Au concentration	808 nm; 1.2 $W.cm^{-2}$ for ≈ 6 min	ΔT= 40.2 °C	67.1%	C6 cells / C6 tumor-bearing mice	[136]
	Organosilica coating onto gold nanostars with conjugation of Gd chelates and functionalized with PEG	Core: 60 nm; Organosilica shell: 20 nm	800 nm	-	808 nm; 0.5 $W.cm^{-2}$ for 10 min	T_{max}= 68.0 ° C	-	MDA-MB-231 cells / MDA-MB-231 tumor-bearing mice	[137]
	Gold nanostar core, MS shell coated with FA	Core: 50 nm; Silica shell: 50-60 nm; Total size: ≈ 150 nm	≈ 800 nm	38.5 µg/mL	808 nm; 800 mW for 5 min	T_{max}= 51.27 °C	31.21 %	HeLa and A549 cells / HeLa tumor-bearing mice	[138]
	Polydopamine coated gold nanostars stabilized with functionalized with PEI	D: 74.2 nm; Silica shell: 18 nm	726 nm	0.35 mM Au concentration	808 nm; 1.3 $W.cm^{-2}$ for 5 min	ΔT= 15.1 °C	40%	HeLa cells / HeLa tumor-bearing mice	[139]
	RGD-modified dendrimer stabilized-gold nanostars	Total size: 55.1 nm	800 nm	20 mM	808 nm; 1.2 $W.cm^{-2}$ for 5 min	ΔT= 55.0 °C	79%	U87MG cells / U87MG tumor-bearing mice	[140]
	Gold nanoshell-coated liposomes containing betulinic acid	Size of the liposomes: 149.4 nm	550-900 nm	58 µg/mL	808 nm; 2.0 $W.cm^{-2}$ for 10 min	T_{max}= 43 °C	-	143B and HeLa cells / U14 tumor-bearing mice	[141]

	Anti-epidermal growth factor receptor antibody-conjugated and paclitaxel loaded-thiol chitosan-layered gold nanoshells	Silica core: 120 nm; Gold nanoshell: 9 nm	700-900 nm	175 μg/mL	808 nm; 1.2 $W.cm^{-2}$ for 5 min	$T_{max} \approx$ 52.5 °C	32.63%	HeLa and MDA-MB231 cells / MDA-MB231 tumor-bearing mice	[104]
	Gold nanoshells onto the silica nanoparticles with dendrimer porphyrin and functionalized with PEI	Size: 186.2 nm	N.D.	-	808 nm; 2.0 $W.cm^{-2}$ for 5 min	$T_{max} \approx$ 62.0 °C	-	HeLa cells	[142]
	Macrophage cell membrane camouflaged Gold Nanoshell Coated MS Nanoparticles	Gold nanoshell: 12 nm; MS: 80 nm; Macrophage membrane: 200 nm	810 nm	1 mg/mL	808 nm; 1.0 $W.cm^{-2}$ for 5 min	ΔT= 30.0 °C	-	4T1 cells / 4T1 tumor-bearing mice	[75]
	Nanoclusters made from ultra-small gold nanoparticles encapsulated into larger spherical polymeric nano constructs of PLGA core stabilized by PEG	Ultra-small nanoparticles: 6 nm; Size: 100 - 180 nm	520 nm	200 μg/mL	800 nm; 100 $J.cm^{-2}$ for 1 min	ΔT= 20.0 °C	-	SUM-159 and U87-MG cells	[143]

	Gold nanocluster-loaded hybrid albumin nanoparticles	Agglomeration of gold nanoparticles with an average size of 4.4 nm	600-900 nm	10 mg/mL	808 nm; 1.5 $W.cm^{-2}$ for 10 min	T_{max}≈ 70.0 °C	-	HCT 116 cells / HCT 116 tumor-bearing mice	[102]
	Core Gold Nanocages shell MS	Ag nanocube L: ≈ 60 nm; Condensed silica layer: ≈ 8 nm; MS: ≈ 25 nm; Total size: 130 nm	530 nm	50 µg/mL	808 nm; 1.0 $W.cm^{-2}$ for 10 min	ΔT= 16.0 °C	-	HeLa cells	[144]
	Double-Walled gold Nanocage/ silica Nanorattles	Ag nanocube: ≈ 35 nm; Gold wall: ≈ 4 nm; Silica layer: 45 nm; Average size: 120 - 130 nm	789 nm	1.20 mg/mL	808 nm, 123.8 $mW.cm^{-2}$ for 10 min	ΔT= 15.3 °C	-	MCF-7 cells	[145]
	MicroRNA-181b into PEI-modified and FR-targeted PEGylated gold nanocages	Gold nanocube: 50 nm; Total Size: 170.6 ± 4.2 nm	802 nm	9.7 µg/mL	808 nm; 1.25 $W.cm^{-2}$ for 10 min	ΔT= 28.2 °C	-	SMMC-7721 cells / SMMC-7721 tumor-bearing mice	[116]

Aims

The main goal of this dissertation work plan was to produce and optimize the synthesis of gold nanoclusters and the coating with a mesoporous silica shell. This approach surpasses the incapacity of gold nanospheres to absorb in the NIR region and consequently enables the application of the gold-core mesoporous silica shell (AuMSS) as photothermal agents. To accomplish that, a new methodology was developed to mediate the aggregation of gold nanospheres in response to incubation with glutathione (GSH). Further, the concentration of tetraethyl orthosilicate (TEOS) was also optimized to produce AuMSS nanoclusters.

The specific aims of this dissertation were:

- Promote the gold nanospheres aggregation;
- Synthesize, optimize, and purify AuMSS nanoclusters;
- Characterization of the AuMSS nanoclusters' physicochemical properties;
- Measurement of the AuMSS nanoclusters' photothermal capacity;
- Evaluation of the AuMSS formulations' biocompatibility;
- Characterization of the nanoparticles' cytotoxic activity (photothermal therapy) using cervical cancer cells as model.

Chapter 2

Experimental Section

2. Experimental Section

2.1. Materials

Hydrogen tetrachloroaurate (III) hydrate ($HAuCl_4$) was purchased from Alfa Aesar (Karlsruhe, Germany). Tetraethyl orthosilicate (TEOS) was bought to Acros Organics (Geel, Belgium). Hexadecyltrimethylammonium bromide (CTAB) were obtained from Tokyo Chemical Industry Europe (Zwijndrecht, Belgium). Hydrochloric acid (HCl) was acquired from Panreac (Barcelona, Spain). Dulbecco's Modified Eagle medium-high glucose (DMEM-HG), Dulbecco's Modified Eagle Medium/Nutrient Mixture F-12 (DMEM-F12), phosphate-buffered saline solution (PBS), ethanol (EtOH), formaldehyde, trypsin, resazurin, and glutathione (GSH) reduced were purchased from Sigma-Aldrich (Sintra, Portugal). Fetal bovine serum (FBS) was bought to Biochrom AG (Berlin, Germany). Calcein acetozxmethyl (calcein AM) and Propidium iodide (PI) were obtained from Invitrogen (Carlsbad, CA). Human negroid cervix epithelioidcarcinoma (HeLa cells) (ATCCs CCL-2TM) were acquired from ATCC (Middlesex, United Kingdom). Primary normal human dermal fibroblast (FibH) cells were bought from Promocell (Heidelberg, Germany). Cell culture t-flasks were obtained from Orange Scientific (Braine-l'Alleud, Belgium). Double deionized and filtered water (ultrapure water) was obtained by using a Milli-Q Advantage A10 Ultrapure Water Purification System (0.22 μm filtered; 18.2 MΩ/cm at 25 °C). Cell imaging plates were acquired from Ibidi GmbH (Munich, Germany).

2.2 Methods

2.2.1. Synthesis of nanospheres

Gold nanospheres were synthesized by adapting a method previously described in the literature [146]. In this one-step reaction, small spherical gold cores are produced by adding, under stirring at 80 °C, 1 mL of formaldehyde (3.7 wt%) and 0.800 mL of $HAuCl_4$ (0.05 M) to 24 ml of ultrapure water (resistivity 18 mΩ) containing 0.05 g of CTAB and NaOH (0.5 M). The resulting solution was left undisturbed for 15 min and then centrifuged (14000 g for 20 min) and resuspended in ultrapure water.

2.2.2. Optimization of the synthesis of AuMSS nanoclusters

2.2.2.1. Production of gold nanoclusters

The synthesis of the different nanoclusters was performed by adding CTAB and GSH to the previous solution. For the study of the effect of different GSH concentrations on the nanoclusters' morphology, different volumes (3; 3.5; 4; 4.5; 5 mL) of GSH solution at 6.13 mg/mL were tested. After 90 min, the resulting solution was centrifuged (11000 g

for 20 min) and resuspended in ultrapure water. Then, 4.56 mg of CTAB, 17.5 μL NaOH (0.5 M), and 0.2 mL of a TEOS solution in ethanol (33% v/v) were added to the previous solution and left to react for 2 h in reflux conditions, originating the mesoporous silica (MS) shell. The produced AuMSS nanoclusters were then recovered by centrifugation at 11000 g and 25 °C. The prepared and purified nanoparticles are referred to as Formula A, B, C, D, and E, for the nanoclusters formed with 3, 3.5, 4, 4.5, and 5 mL of GSH, respectively.

From the previous formulations, the two that presented the best results in TEM and UV-vis characterization (3.5 mL and 5 mL of GSH) were selected for optimization of the mesoporous silica shell. For that purpose, the previously described methodology was adapted by adjusting the amount of TEOS (33% v/v in ethanol) added to the synthesis 0.200, 0.100, or 0.050 mL (please see table 2).

Table 2: Summary of GSH and TEOS optimization during the production of different formulations of AuMSS nanoclusters.

GSH (mL)	TEOS (mL)	Formula
3	200	A
3.5	200	B
4	200	C
4.5	200	D
5	200	E
3.5	50	F
3.5	100	G
5	50	H
5	100	I

2.2.3. Removal of surfactant template

The extraction of the cytotoxic CTAB template from the AuMSS nanoclusters was performed by adapting a solvent-based approach described in the literature [147]. Briefly, several washing steps were performed by resuspending the gold mesoporous nanoclusters in an acidic solution (HCl 7.5% v/v in ethanol) and sonicating them for 1 min. After, the nanoparticles were washed several times with absolute ethanol at 4 °C, to allow the complete removal of the CTAB and HCl residues. Finally, the particles were resuspended in ultrapure water, recovered by centrifugation (14000 g for 20 min), and freeze-dried.

2.2.4. Characterization of nanocarriers' physicochemical properties

2.2.4.1. Morphological characterization

The morphology of AuMSS nanoclusters was characterized by Transmission Electron Microscopy (TEM –Hitachi-HT7700, Japan). The samples were placed on formvar-coated copper grids and dried at room temperature. The images were acquired at an accelerating voltage of 80 kV.

2.2.4.2. Size and zeta potential analysis

The AuMSS nanoclusters' size and zeta potential were evaluated using a Zetasizer Nano ZS equipment (Malvern Instruments, Worcestershire, United Kingdom). In all measurements, the nanoparticles were resuspended in ultrapure water, and the data was collected at 25 ºC in a disposable capillary cell.

2.2.4.3. Ultraviolet-visible spectroscopy analysis

The success of AuMSS nanoclusters synthesis was evaluated by acquiring the UV-vis spectra in a UV-Vis spectrophotometer (Thermo Scientific Evolution™ 201 Bio UV-vis Spectrophotometer, Thermo Fisher Scientific Inc., USA). The UV-vis spectra of the nanoclusters were recorded at 300nm/min scanning rate, with a wavelength range from 300 to 1100 nm.

2.2.4.4. *In vitro* photothermal measurements

The evaluation of the AuMSS nanoclusters' *in vitro* photothermal capacity was performed as previously described in the literature [146]. Briefly, nanoparticles at a concentration of 200 μg/mL and a control group without particles were irradiated with a NIR laser (808 nm, 1.7 $W.cm^{-2}$ for 5 min). Then, the variation of the solution temperature was measured at different time points (from 1 up to 10 min) by using a thermocouple sensor with an accuracy of 0.1 ºC.

2.2.5. Cytocompatibility assay

The biocompatibility of the different formulations of AuMSS nanoclusters was evaluated through a resazurin-based assay at different time points. This method uses a non-toxic reagent (resazurin), which when inside the cells is reduced from a non-fluorescent blue resazurin compound to the fluorescent pink-reddish resorufin. This transformation occurs through the action of mitochondrial enzymes such as flavin mononucleotide dehydrogenase and nicotinamide adenine dehydrogenase [148].

HeLa and FibH cells were seeded in 96-well flat-bottom culture plates at a density of 10000 cells per well, with 100 μL of culture medium (DMEM-HG) during 48 h, at 37 ºC,

in a humidified atmosphere containing 5% CO_2. After that time, cells were incubated with different concentrations (50 to 200 µg/mL) of AuMSS nanoclusters formulation. After 24, 48, and 72 h of incubation, the medium was replaced with 110 µL of 10% (v/v) resazurin solution and incubated for 4 h. The produced resorufin fluorescence was quantified with a spectrofluorometer (Spectramax Gemini XS, Molecular Devices LLC, USA) at an excitation/emission wavelength of λex=560 nm and λem=590 nm. Cells incubated with absolute EtOH were used as a positive control (K^+), whereas cells without being exposed to nanoparticles were used as a negative control (K^-).

2.2.6. Characterization of the nanoclusters phototherapeutic effect

2.2.6.1 Characterization of the 2D cytotoxic activity of the nanoparticles

The NIR induced cytotoxic activity of AuMSS nanoclusters upon 1 or 3 irradiations cycles with NIR light was evaluated through the resazurin assay. Briefly, 10 000 HeLa cells were seeded in 96-well plates containing DMEM-HG culture medium. Then, the different formulations of AuMSS nanoclusters (Formula F, G, H, and I) were incubated with HeLa cells. After 6 h, the cells were submitted to 1 or 3 cycles of irradiation with a NIR laser (808 nm, 1.7 W/cm² for 5 min). After 24 h of incubation, the cell viability was assessed by using the resazurin assay. Cells incubated with EtOH (99.9% v/v) were used as a positive control (K^+) whereas cells without being exposed AuMSS nanoclusters were used as negative controls (K^-).

2.2.6.2. HeLa cells live/dead assay

The photothermal potential of AuMSS nanoclusters was also evaluated by fluorescence microscopy using the Live/Dead assay (Invitrogen, Life Technologies, USA). This assay uses Calcein acetoxymethyl (Calcein AM) and PI dyes to allow visualization of living and dead cells, respectively. For that purpose, HeLa cells were seeded on µ-Slide 8 well Ibidi imaging plates (Ibidi GmbH, Germany), and incubated at 37 °C, in a humid atmosphere at 5% CO_2 for 24 h. After this period, the different formulations of AuMSS nanoclusters at a concentration of 200 µg / mL were incubated with HeLa cells, while cells non-exposed to nanoparticles were used as a negative control (Control). After 48 h, the cells were incubated with the staining solution according to the manufacturer's instructions and analyzed under a confocal microscope (Zeiss LSM 710, Carl Zeiss, Germany).

2.2.7. Statistical analysis

Statistical analysis of the obtained results was performed using GraphPad Prism v.6.0 software (Trial version, GraphPad Software, CA, USA). Data are presented as the mean ± standard deviation (s.d.). One-way analysis of variance (ANOVA) with the Student–Newman–Keuls test was used to compare different groups. A value of $p < 0.05$ was considered statistically significant.

Chapter 3

Results and Discussion

3. Results and Discussion

3.1. Evaluation of the GSH effect on the agglomeration of gold nanoparticles

The main goal of this study was to develop and optimize a new method to produce gold nanoclusters coated with a mesoporous silica shell. The AuMSS nanoclusters production can be divided into three main phases: i) synthesis of gold nanospheres; ii) agglomeration of gold nanospheres; and iii) coating with a mesoporous silica shell (Figure 4).

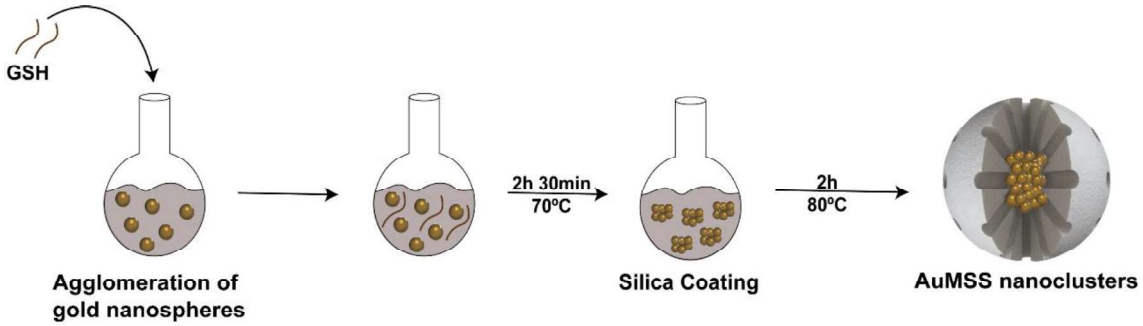

Figure 4: Representation of the nanoclusters' optimization synthesis.

The gold nanospheres were synthesized by adapting a method previously described in the literature based on the gold reduction in the presence of formaldehyde [146]. Afterward, GSH was selected to mediate the nanospheres agglomeration due to previous evidence on literature that compounds containing amine and thiol functional groups can trigger the aggregation of gold nanoparticles [149]. In fact, it is well described in the literature the gold affinity to interact with molecules composed of thiol functional groups. Therefore, the establishment of gold-thiol interactions can allow the GSH to act as a molecular bridge triggering the gold nanospheres aggregation. Finally, the gold nanoclusters are coated with a mesoporous silica shell by promoting the hydrolysis of TEOS in the presence of CTAB.

The GSH contribution to the agglomeration of gold nanospheres was studied by adding increasing amounts 3, 3.5, 4, 4.5, and 5 mL of GSH (6.13 mg/mL) to the gold nanospheres solution. Then, the newly formed gold nanoclusters were coated with a mesoporous silica shell through the addition of TEOS (0.2 mL at 33% v/v in ethanol) resulting in the Formula A, B, C, D, and E according to the added GSH, 3, 3.5, 4, 4.5, and 5 mL respectively. The successful agglomeration of the gold nanoparticles was preliminarily confirmed by TEM, as shown in Figure 5. The analysis of the TEM image demonstrates

the successful formation of gold nanoclusters after reaction with GSH and confirmed the core-shell organization of the nanoparticles. Moreover, the TEM images also show that Formula B and E AuMSS nanoclusters present a lower quantity of non-coated gold nanoclusters (Figure 6).

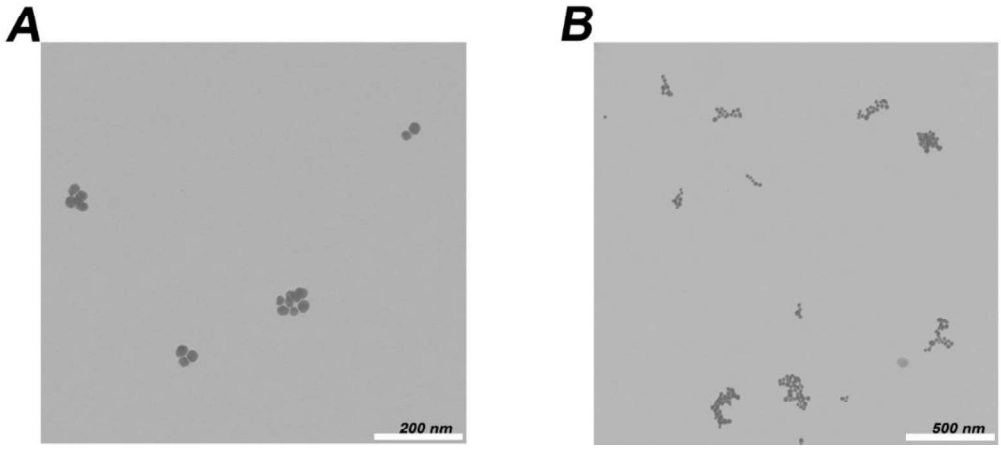

Figure 5: TEM images of gold nanospheres aggregation. 3.5 mL (A) and 5 mL (B) of GSH.

Apart from the morphological characterization, the UV-vis spectra were also acquired to assess any possible alterations in the AuMSS absorption spectra. The obtained results show a slight redshift in the absorption peak of gold nanoclusters as well as an overall increase in the absorption capacity in the 700-800 nm region when compared to gold nanospheres (Figure 6F). Further, in general, an increase in the GSH amount resulted in a higher absorption in the NIR region of the spectra, which is advantageous for the application of AuMSS nanocluster in PTT. These changes in the gold nanoclusters absorption spectra are attributed to the interactions of the free electrons on the particle's surface with the adjacent ones in close proximity promoting the coupling of the plasmon resonances [150].

Considering both TEM and UV-vis data, Formula B and E AuMSS nanoclusters were selected as the most promising for further testings, silica shell optimization, due to the increased particle uniformity (*i.e.* lower number of non-coated gold clusters) and enhanced NIR absorption.

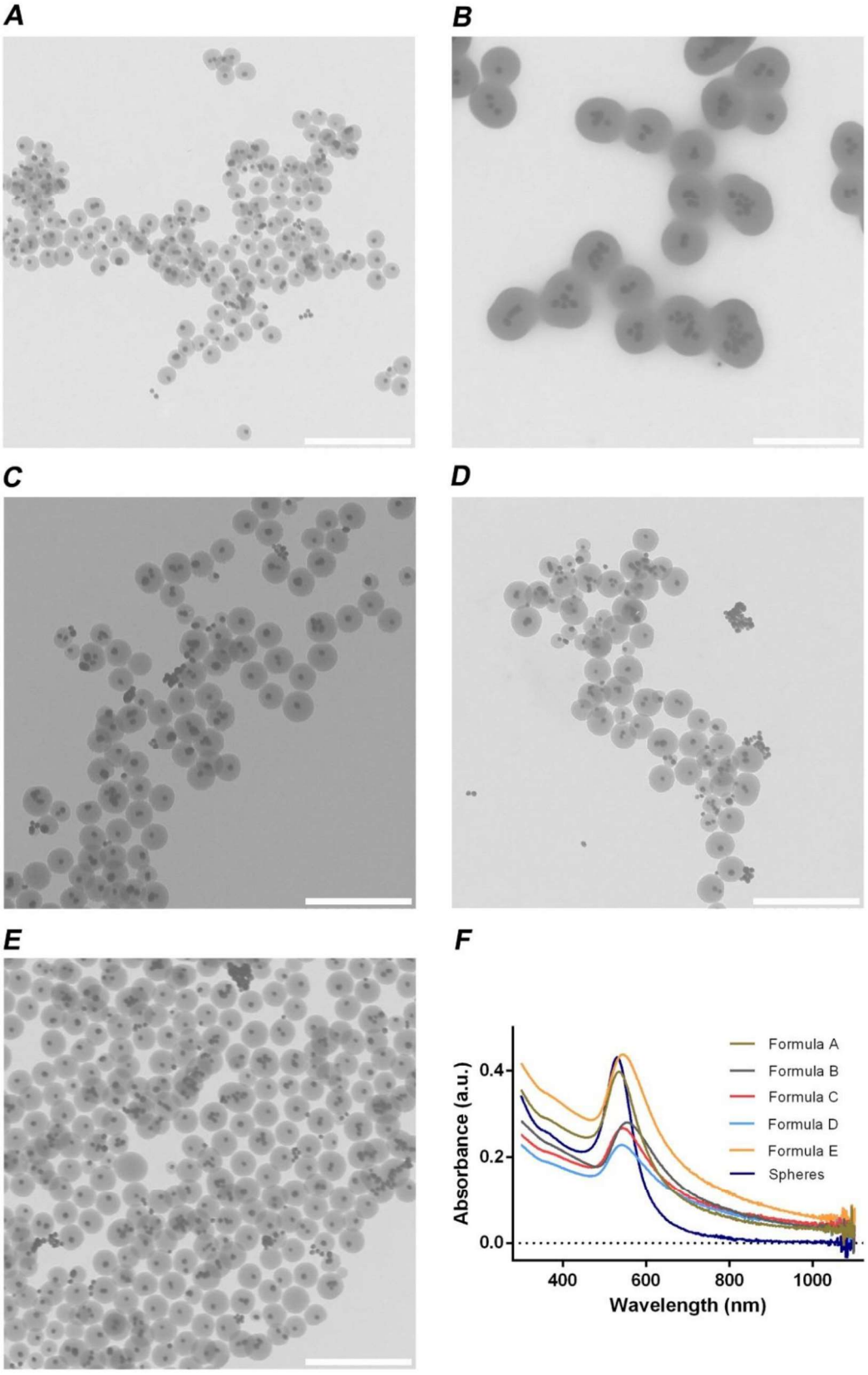

Figure 6: AuMSS nanoclusters morphology and UV-vis data analysis. TEM images of Formula A (A), Formula B (B), Formula C (C), Formula D (D), and Formula E (E) AuMSS nanoclusters. UV-vis spectra of different nanoformulations of AuMSS nanoclusters (F). Scale bar: 500 nm.

3.2. Optimization of the mesoporous silica shell

The introduction of a mesoporous silica shell can also impact the physicochemical properties of the gold nanoparticles [38]. With that in mind, the mesoporous silica coating was optimized by fine-tuning the TEOS concentration. For that purpose, gold nanoclusters produced using 3.5 or 5 mL of GSH (6.13 mg/mL) were reacted with 0.200, 0.100, or 0.50 mL of TEOS (33% v/v in ethanol). The Formula B, G, and F refer to the AuMSS nanoclusters produced using 3.5 mL of GSH (6.13 mg/mL) and 0.200, 0.100, or 0.50 mL of TEOS, respectively, whereas the Formula E, I, and H represent the ones resulting from 5 mL of GSH (6.13 mg/mL) and 0.200, 0.100, or 0.50 mL of TEOS, respectively.

The produced Formula B, E, F, G, H, and I AuMSS nanoclusters were characterized by DLS to assess their size and particle distribution, Figure 7. The AuMSS nanoclusters have a homogeneous population and the reduction in the TEOS amount generally resulted in the decrease of the nanoparticles' mean size. The AuMSS nanoclusters produced with 3.5 mL of GSH presented a mean diameter of 267.74, 202.86, and 136 nm for Formula B, F, and G, respectively. Otherwise, Formula E, H, and I nanoclusters presented a mean diameter of 109.20, 91.58, and 89.67 nm, respectively. This size reduction within each nanocluster group might be justified by the reduction of the mesoporous silica shell thickness in response to the decrease in the silica source, *i.e.* TEOS, during the synthesis process. Additionally, this TEOS optimization also originates nanomaterials with size within the range considered ideal for intravenous administration (*i.e.* 100 to 200 nm) and favoring the passive accumulation in the tumor tissue by exploiting the leaky structure of the tumoral vasculature, *i.e.* the EPR effect [38, 71].

Otherwise, surface charge measurements were also performed to further characterize the surface of the nanoparticles. The obtained results show that all the different formulations present a negative surface charge (Figure 7G), which is attributed to the silanol groups available at the surface of the AuMSS nanoclusters. Additionally, this negative surface charge is also indicative of the successful removal of the cationic CTAB molecules used both as structure-directing agents for the pores formation and surfactant for maintaining the stability of the particles [88, 151]. CTAB removal is an important step in the development of silica-based nanomaterials due to the high cytotoxicity of this surfactant. Furthermore, nanomaterials with slightly negative surface charges often translate to increased blood circulation times due to the reduced interactions with blood cellular components and serum proteins [152].

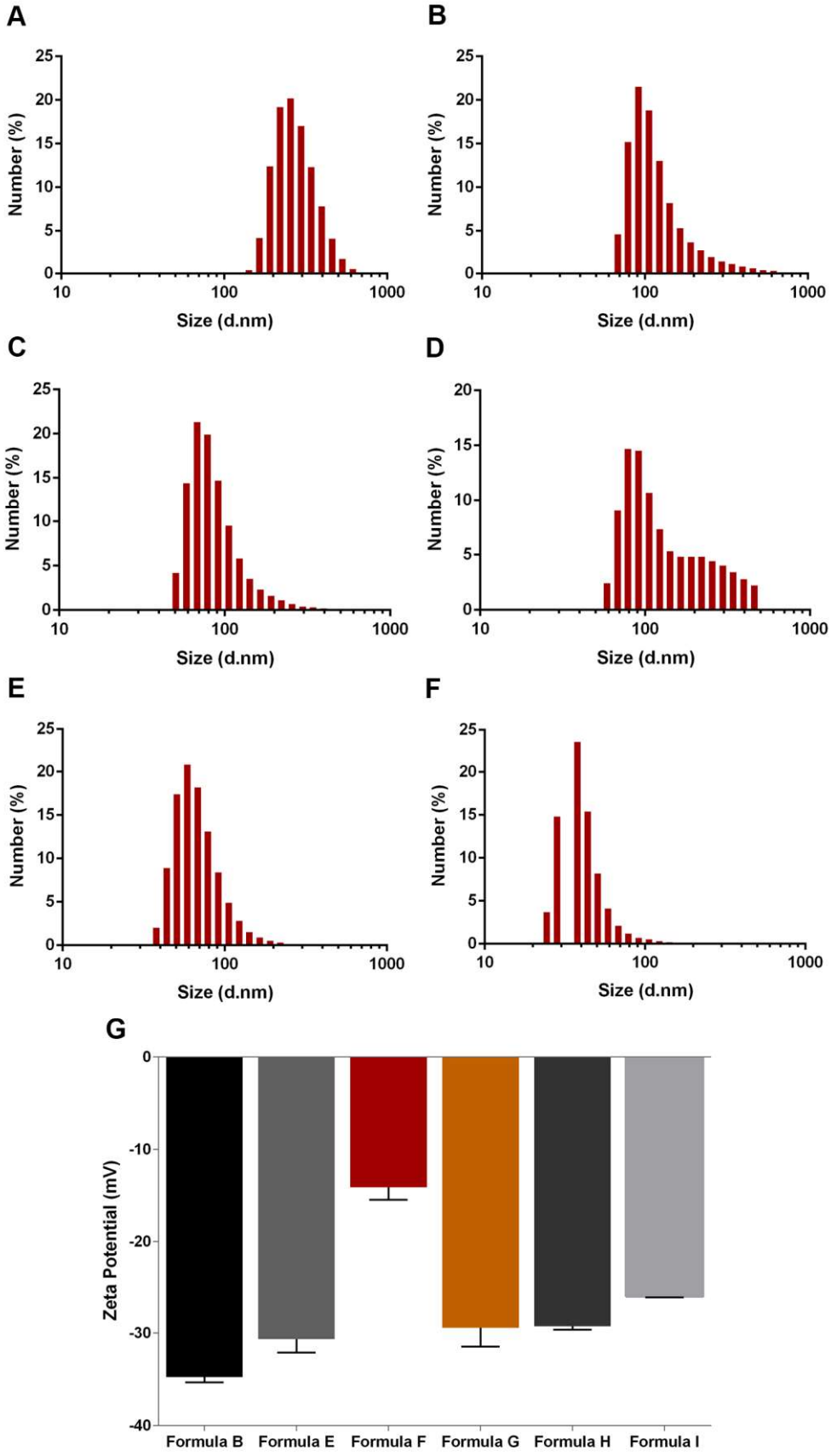

Figure 7: Physicochemical characterization of AuMSS nanoclusters formulations. The size distribution of Formula B (A), Formula E (B), Formula F (C), Formula G (D), Formula H (E), and Formula I (F), n=300. (G) Surface charge analysis of all AuMSS nanoclusters formulations, n=3.

3.3. *In vitro* evaluation of the photothermal capacity

The AuMSS nanoclusters' potential to act as a photothermal agent was initially assessed by acquiring the UV-vis absorption spectra of Formula B, E, F, G, H, and I (Figure 8A). As previously observed, the organization of gold nanospheres into nanoclusters induced redshift in the absorption peak and enhanced the absorption capacity in the 700-800 nm region [96-98]. Particularly, Formula G, H, and I nanoclusters present a broad absorption peak from the 500 to 800 nm region. Moreover, the obtained data also show that decreasing the TEOS amount during the AuMSS nanocluster synthesis further increases the absorption capacity in the NIR region. The analysis of the absorption spectra revealed that in the AuMSS nanoclusters produced with 3.5 mL of GSH, the TEOS reduction from 0.200 to 0.100 and 0.050 mL (Formula B, G, and F) enhanced the absorption at 808 nm in 403 and 154%, respectively. Similar results were observed in the AuMSS nanoclusters produced with 5 mL of GSH with a 363 and 311% increase in the absorption at 808 nm for the Formula H and I, respectively. Considering the different formulations of AuMSS nanoclusters, it is possible to conclude that Formula H AuMSS nanoclusters (*i.e.* 5 mL of GSH and 0.050 mL of TEOS) are the ones presenting the highest absorption in the NIR region. Nevertheless, the overall enhancement of the absorption in the NIR region with the TEOS optimization further supports the applicability of AuMSS nanocluster in PTT applications.

Then, the photothermal capacity of AuMSS nanoclusters was investigated by recording the temperature changes upon the exposition of these nanomaterials to NIR light (808 nm, 1.7 W cm^{-2}) for a maximum of 10 min (Figure 8B). The obtained results demonstrated that all the AuMSS nanoclusters can generate heat and increase the temperature of the surrounding media in response to the irradiation with a NIR laser. From all the tested formulations, Formula B and E (0.200 mL of TEOS) induced the smallest increase in temperature, *i.e.* $\Delta T \approx 8$ ºC. Otherwise, the NIR laser irradiation of the Formula H and I AuMSS nanoclusters resulted in the highest temperature increase, $\Delta T \approx 20$ and 13 ºC, respectively. In turn, the Formula F and G AuMSS nanoclusters mediated a temperature increase of ≈ 11 ºC. Despite the differences in the maximum temperature, all the AuMSS nanoclusters presented similar heating profiles upon NIR laser irradiation, with a pronounced temperature increase in the first 5 min of irradiation followed by a temperature stabilization until the end of the experiment. It is worth to notice, that the differences observed in the heating capacity of the different AuMSS nanoclusters are in accordance with the results previously obtained in the absorption spectra. More importantly, the heat generated in response to the irradiation with the NIR indicates that these AuMSS nanoclusters can be explored to trigger the death of cancer

cells by inducing the disruption of the cell membrane as well as alterations on the metabolic pathways.

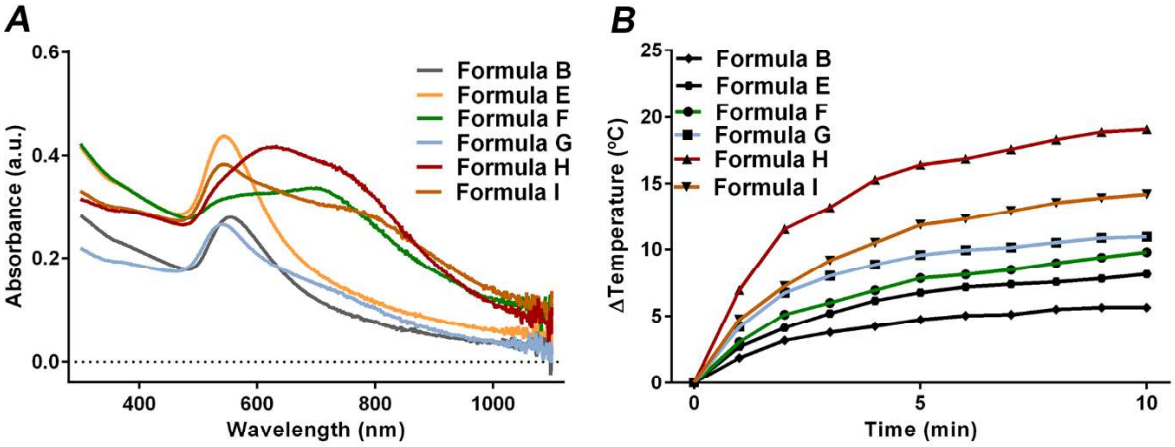

Figure 8: Characterization of the PTT capacity of AuMSS nanoclusters. (A) UV-vis spectra of different nanoformulations of AuMSS nanoclusters. (B) Temperature variation curve of AuMSS nanoclusters in complex in ultrapure water, NIR laser (808 nm, 1.7 $W.cm^{-2}$) irradiation for 10 min. Data are presented as mean ± s.d., * $p < 0.05$, $n = 3$.

3.4. Nanoparticles biocompatibility

3.4.1. Cell viability

The nanomaterials' biocompatibility is paramount to allow their application in the biomedical field. The biocompatibility of AuMSS nanoclusters was evaluated both on FibH and HeLa cells (Figure 9). For that purpose, the different formulations of AuMSS nanoclusters were incubated for 24, 48, and 72 h, at concentrations ranging from 50 up to 200 μg/mL, and the cellular viability was measured using the resazurin assay. According to the ISO 10993-5 "Biological evaluation of medical devices -Part 5: Tests for *in vitro* cytotoxicity", a material has a cytotoxic effect when the cell viability is reduced by more than 30%. Therefore, the obtained results show that all the different AuMSS nanoclusters formulations are biocompatible at concentrations up to 200 μg/mL for both cell lines. Therefore, this data further supports the successful removal of CTAB from the AuMSS nanoclusters during the purification step, it is worth to notice that the CTAB is more cytotoxic than DOX (an anticancer drug with a broad spectrum of activity) [153]. Additionally, these results are in concordance with other reports available in the literature for gold core-silica shell-based nanomedicines [154, 155].

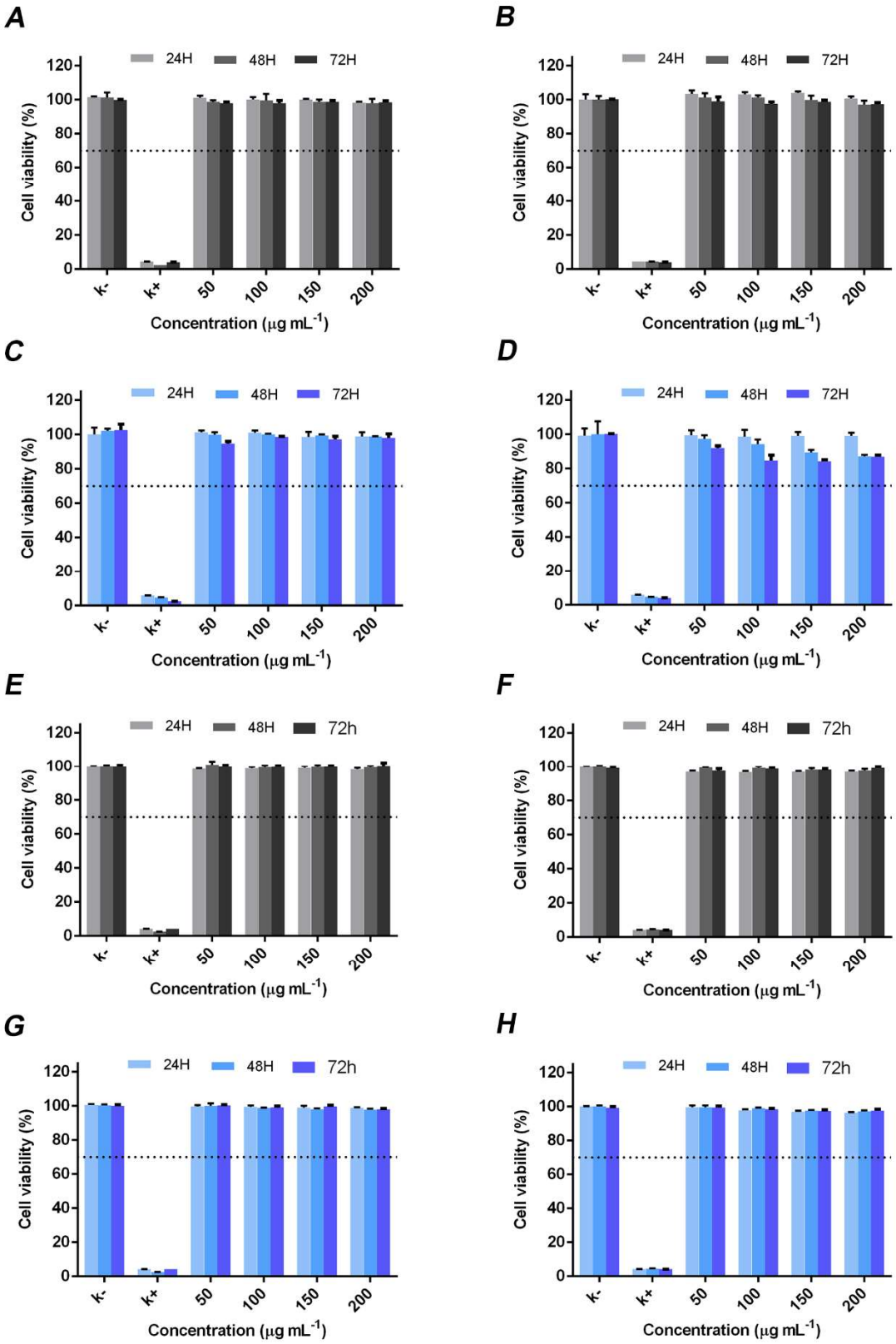

Figure 9: Evaluation of AuMSS nanoformulations' cytocompatibility at 24, 48, and 72 h on HeLa (A, C, E, and G) and FibH cells (B, D, F, and H). Cytocompatibility analysis for AuMSS nanoclusters of Formula B (A) and (B), Formula E (C) and (D), Formula H (E) and (F), and Formula I (G) and (H). Positive control (K^+): cells treated with EtOH; negative control (K^-): cells without nanoparticle incubation. Data are presented as mean ± s.d.

3.4.2. Photothermal effect mediate by AuMSS nanoclusters

The Formula F, G, H, and I were selected to evaluate the PTT potential of AuMSS nanoclusters since these formulations presented the best results in the *in vitro* photothermal measurements. The AuMSS nanoclusters cytotoxic profile towards HeLa cells was assessed upon 1 or 3 cycles of irradiation with NIR light (Figure 10). For that purpose, the cells were incubated with the different formulations of AuMSS nanoclusters at a concentration of 200 µg/mL and irradiated with the NIR laser (808 nm, 1.7 $W.cm^{-2}$, for 10 min). The obtained results show that the heat generated by the AuMSS nanoclusters under NIR laser irradiation induces the reduction of the HeLa cells' viability. Moreover, the increase in the number of NIR laser irradiation cycles further enhanced the AuMSS nanoclusters' capacity to induce the death of cancer cells. It is worth to notice that the Formula H and I AuMSS nanoclusters presented the highest reduction in the HeLa cells viability reaching values inferior to 25% and 60% after 3 cycles of irradiation, respectively. Such data is in agreement with the *in vitro* photothermal measurements, where these two formulations mediated the highest increase in the media temperature. Hyperthermia treatments that reach temperatures above 45 °C can induce the death of cancer cells by causing irreversible damages to DNA, protein denaturation, and the rupture of cell membranes [37].

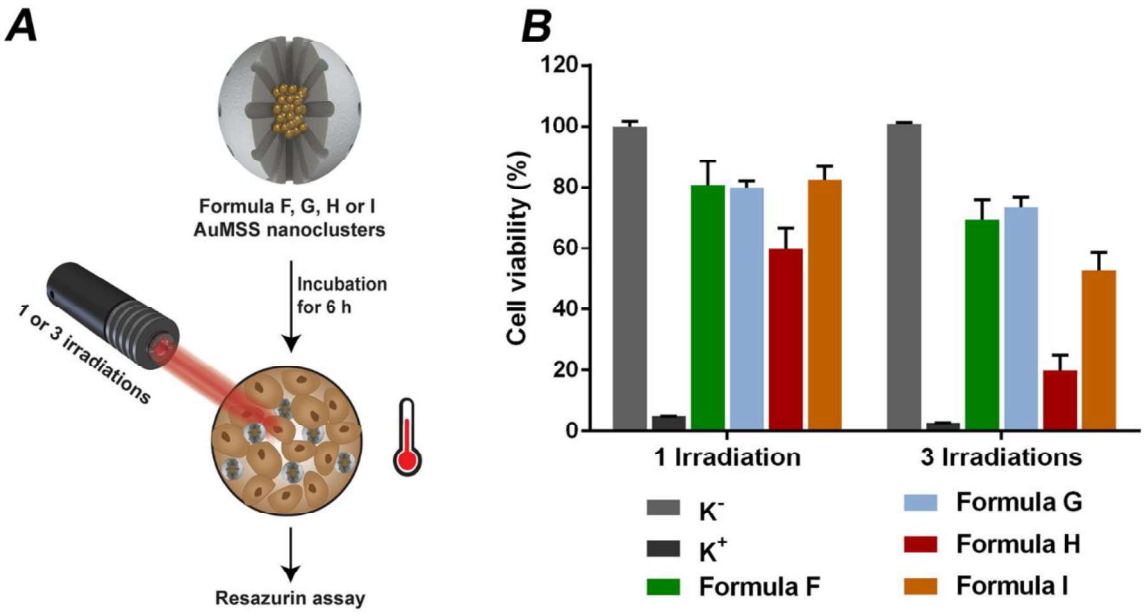

Figure 10: AuMSS nanoclusters cytotoxic profile towards HeLa cells. (A) Schematic representation of AuMSS nanoclusters cytotoxic activity upon NIR irradiation (808 nm, 1.7 W/cm^2, 5 min). (B) Cytotoxic activity of different nanoclusters at 200 µg/mL with 1 and 3 laser irradiations.

The AuMSS nanoclusters' photothermal therapeutic effect was further confirmed by the Confocal Laser Scanning Microscopy (CLSM) images of the Live/Dead assays. In this assay, the HeLa cells were stained with Calcein AM and PI after incubation with the different AuMSS nanocluster formulations and 1 or 3 cycles of irradiation with NIR light. In Figure 11, it is possible to observe a large area of dead cells (*i.e.* red fluorescence) in the region irradiated with the NIR laser. Further, it is possible to observe that the area of dead cells increases with the number of irradiation cycles, supporting the data obtained in the resazurin assays. Therefore, the reduction of the HeLa cells viability and the Live/Dead images confirm that the AuMSS nanoclusters can mediate an on-demand photothermal therapeutic effect upon NIR laser irradiation.

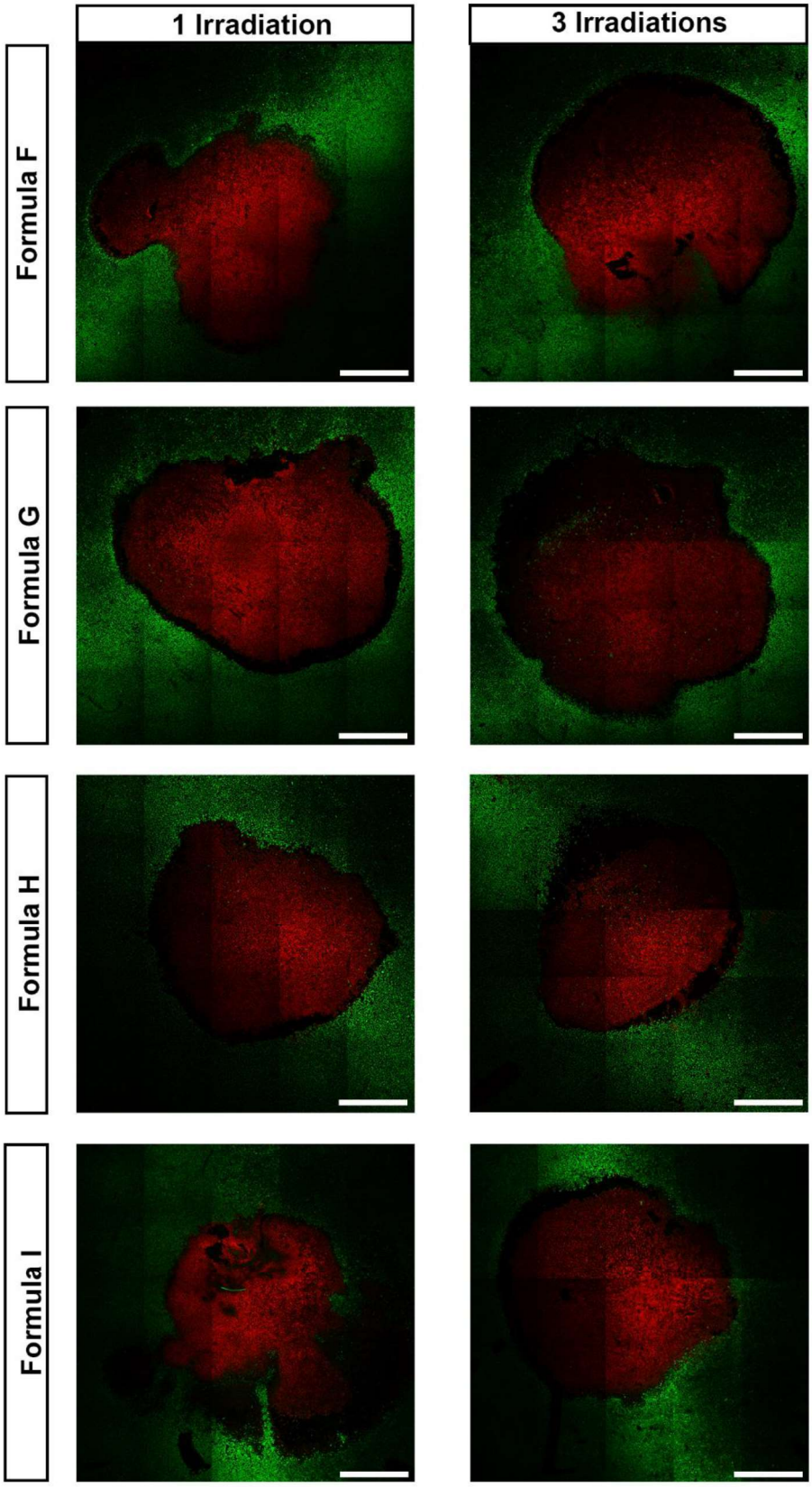

Figure 11: Cytotoxic effect of AuMSS nanoformulations in HeLa cells. Live/Dead CLSM images of the cytotoxic activity of different nanoclusters at 200 μg/mL with 1 and 3 laser irradiations. Green Channel: Calcein stained cells; Red channel: PI stained cells. Scale bar: 200 μm.

Chapter 4

Conclusion and Future Perspectives

4. Conclusion and Future Perspectives

Nowadays, despite all the efforts, cancer remains a major health problem affecting the world's population. In this field, the breakthroughs of nanotechnology rendered the development of novel and more effective anticancer therapies. Among them, the AuMSS nanoparticles display advantageous physicochemical and biological properties that make them promising nanoplatforms for cancer therapy. The core-shell organization of AuMSS allows the combination of the imaging and photothermal capacity of gold nanomaterials with the superior stability and drug loading ability of mesoporous silica.

Herein, a new methodology was optimized to produce AuMSSs composed of a core of gold nanoclusters, to overcome the incapacity of gold nanospheres to absorb radiation in the NIR region and consequently enable the application of the AuMSS as photothermal agents. The development of the AuMSS nanoclusters was based on the optimization of two main parameters, the amount of GSH (*i.e.* the agent responsible for mediating the gold nanospheres aggregation) and silica source (*i.e.* TEOS). The obtained results revealed that the increase in the nanoclusters formation and the absorption capacity in the 700-800 nm with crescent amounts of GSH. Among them, the AuMSS nanoclusters produced with 3.5 and 5 mL of GSH (Formula B and E) were selected for further studies since these two formulations presented the best compromise between the amount of non-coated gold nanoclusters and absorption in the NIR region. Then, the formation of the mesoporous silica shell was optimized in the two selected formulations of AuMSS nanoclusters. The reduction in the silica source (from 0.200 to 0.100 and 0.050 mL) during the AuMSS nanoclusters synthesis resulted in the fine-tuning of the nanomaterials' size to values within the range considered ideal for intravenous administration (*i.e.* 100 to 200 nm). Further, it was also observed a significant enhancement in the absorption capacity at 808 nm, 1.5-4 times higher, in the Formula G, F, H, and I AuMSS nanoclusters. Such improvements resulted in higher photothermal capacities, reaching the maximum ΔT of $\approx$ 20 and 13 ^{o}C with the Formula H and I, respectively. Furthermore, all the AuMSS nanoclusters were biocompatible with FibH and HeLa cells at concentrations up to 200 μg /mL. Finally, the Formula G, F, H, and I AuMSS nanoclusters shown an on-demand photothermal effect that induced the death of HeLa cancer cells with the NIR laser irradiation, which was further enhanced when multiple irradiations were used. Overall, the obtained data support the application of AuMSS nanoclusters as PTT agents, particularly Formula H, which presented the highest heat generation and consequent reduction in the HeLa cells viability.

In the future, the complete characterization of the drug loading and release profile at both physiological and acidic pH will be performed to evaluate the AuMSS nanoclusters' potential to mediate the chemo-photothermal combinatorial anticancer effect, further increasing the particles therapeutic potential. Additionally, the introduction of targeting moieties (*e.g.* folate, hyaluronic acid, and aptamers) is also envisioned to increase the AuMSS nanoclusters' specificity towards the HeLa cancer cells. Finally, the evaluation of the therapeutic performance of these nanoformulations in tumor spheroids will be essential to proceed to the *in vivo* tests.

Chapter 5

References

5. References

1. Siegel, R.L., K.D. Miller, and A. Jemal, *Cancer statistics, 2020*. CA: A Cancer Journal for Clinicians, 2020. **70**(1): p. 7-30.
2. Miranda N, Gonçalves MB, Andrade C, Santos G. Programa nacional para as doenças oncológic*as 2017*. 2017, Direção Geral de Saúde.
3. Drake, I., et al., *Lifestyle and cancer incidence and mortality risk depending on family history of cancer in two prospective cohorts*. International Journal of Cancer, 2020. **146**(5): p. 1198-1207.
4. *Cancer Facts & Figures*. American Cancer Society, 2020.
5. Forouzanfar, M.H., et al., *Global, regional, and national comparative risk assessment of 79 behavioural, environmental and occupational, and metabolic risks or clusters of risks, 1990–2015: a systematic analysis for the Global Burden of Disease Study 2015*. The lancet, 2016. **388**(10053): p. 1659-1724.
6. Floor, S.L., et al., *Hallmarks of cancer: of all cancer cells, all the time?* Trends in molecular medicine, 2012. **18**(9): p. 509-515.
7. Pan, M.-H., et al., *Multistage carcinogenesis process as molecular targets in cancer chemoprevention by epicatechin-3-gallate*. Food & function, 2011. **2**(2): p. 101-110.
8. Kidd, S., et al., *Origins of the tumor microenvironment: quantitative assessment of adipose-derived and bone marrow–derived stroma*. PloS one, 2012. **7**(2).
9. Hanahan, D. and L.M. Coussens, *Accessories to the crime: functions of cells recruited to the tumor microenvironment*. Cancer cell, 2012. **21**(3): p. 309-322.
10. Xiong, Y., et al., *Hematopoietic stem cell-derived adipocytes and fibroblasts in the tumor microenvironment*. World journal of stem cells, 2015. **7**(2): p. 253.
11. Bussard, K.M., et al., *Tumor-associated stromal cells as key contributors to the tumor microenvironment*. Breast Cancer Research, 2016. **18**(1): p. 84.
12. Choi, H. and A. Moon, *Crosstalk between cancer cells and endothelial cells: implications for tumor progression and intervention*. Archives of pharmacal research, 2018. **41**(7): p. 711-724.
13. Zamarin, D., et al., *Localized oncolytic virotherapy overcomes systemic tumor resistance to immune checkpoint blockade immunotherapy*. Science translational medicine, 2014. **6**(226): p. 226ra32-226ra32.
14. Witsch, E., M. Sela, and Y. Yarden, *Roles for growth factors in cancer progression*. Physiology, 2010. **25**(2): p. 85-101.
15. Pickup, M., S. Novitskiy, and H.L. Moses, *The roles of TGFβ in the tumour microenvironment*. Nature Reviews Cancer, 2013. **13**(11): p. 788-799.

16. Malumbres, M. and M. Barbacid, *Cell cycle, CDKs and cancer: a changing paradigm*. Nature reviews cancer, 2009. **9**(3): p. 153-166.
17. Kim, M.P., Y. Zhang, and G. Lozano, *Mutant p53: multiple mechanisms define biologic activity in cancer*. Frontiers in oncology, 2015. **5**: p. 249.
18. Shay, J.W., *Role of telomeres and telomerase in aging and cancer*. Cancer discovery, 2016. **6**(6): p. 584-593.
19. Folkman, J., *Tumor angiogenesis: therapeutic implications*. New england journal of medicine, 1971. **285**(21): p. 1182-1186.
20. Hanahan, D. and R.A. Weinberg, *Hallmarks of cancer: the next generation*. cell, 2011. **144**(5): p. 646-674.
21. Brahimi-Horn, M.C., J. Chiche, and J. Pouysségur, *Hypoxia and cancer*. Journal of molecular medicine, 2007. **85**(12): p. 1301-1307.
22. Yang, Y., et al., *HIFs, angiogenesis, and cancer*. Journal of cellular biochemistry, 2013. **114**(5): p. 967-974.
23. Carmeliet, P. and R.K. Jain, *Angiogenesis in cancer and other diseases*. nature, 2000. **407**(6801): p. 249-257.
24. Fraisl, P., et al., *Regulation of angiogenesis by oxygen and metabolism*. Developmental cell, 2009. **16**(2): p. 167-179.
25. Singh, N., et al., *Inflammation and cancer*. Annals of African medicine, 2019. **18**(3): p. 121.
26. Grivennikov, S.I. and M. Karin, *Inflammation and oncogenesis: a vicious connection*. Current opinion in genetics & development, 2010. **20**(1): p. 65-71.
27. Yeung, S., J. Pan, and M.-H. Lee, *Roles of p53, MYC and HIF-1 in regulating glycolysis—the seventh hallmark of cancer*. Cellular and Molecular Life Sciences, 2008. **65**(24): p. 3981.
28. Liang, C., W. Chao, and L. Zhuang, *Functional nanomaterials for phototherapies of cancer*. Chinese Journal of Clinical Oncology, 2014(1): p. 18-26.
29. Datta, N., et al., *Local hyperthermia combined with radiotherapy and-/or chemotherapy: Recent advances and promises for the future*. Cancer treatment reviews, 2015. **41**(9): p. 742-753.
30. Pardoll, D.M., *The blockade of immune checkpoints in cancer immunotherapy*. Nature Reviews Cancer, 2012. **12**(4): p. 252-264.
31. Robertson, C.A., D.H. Evans, and H. Abrahamse, *Photodynamic therapy (PDT): a short review on cellular mechanisms and cancer research applications for PDT*. Journal of Photochemistry and Photobiology B: Biology, 2009. **96**(1): p. 1-8.

32. Kong, G. and M. Dewhirst, *Review hyperthermia and liposomes*. International Journal of Hyperthermia, 1999. **15**(5): p. 345-370.
33. Wust, P., et al., *Hyperthermia in combined treatment of cancer*. The lancet oncology, 2002. **3**(8): p. 487-497.
34. Chatterjee, D.K., P. Diagaradjane, and S. Krishnan, *Nanoparticle-mediated hyperthermia in cancer therapy*. Therapeutic delivery, 2011. **2**(8): p. 1001-1014.
35. Beik, J., et al., *Nanotechnology in hyperthermia cancer therapy: From fundamental principles to advanced applications*. Journal of Controlled Release, 2016. **235**: p. 205-221.
36. Kumar, C.S. and F. Mohammad, *Magnetic nanomaterials for hyperthermia-based therapy and controlled drug delivery*. Advanced drug delivery reviews, 2011. **63**(9): p. 789-808.
37. de Melo-Diogo, D., et al., *Strategies to improve cancer photothermal therapy mediated by nanomaterials*. Advanced Healthcare Materials, 2017. **6**(10): p. 1700073.
38. Moreira, A.F., D.R. Dias, and I.J. Correia, *Stimuli-responsive mesoporous silica nanoparticles for cancer therapy: A review*. Microporous and Mesoporous Materials, 2016. **236**: p. 141-157.
39. Terentyuk, G.S., et al., *Laser-induced tissue hyperthermia mediated by gold nanoparticles: toward cancer phototherapy*. Journal of biomedical optics, 2009. **14**(2): p. 021016.
40. Kislev, H., *Nanoparticle mediated ultrasound therapy and diagnostic imaging*. 2008, Google Patents.
41. Obaidat, I.M., B. Issa, and Y. Haik, *Magnetic properties of magnetic nanoparticles for efficient hyperthermia*. Nanomaterials, 2015. **5**(1): p. 63-89.
42. Pekkanen, A.M., M.R. DeWitt, and M.N. Rylander, *Nanoparticle enhanced optical imaging and phototherapy of cancer*. Journal of biomedical nanotechnology, 2014. **10**(9): p. 1677-1712.
43. Zhou, J., et al., *NIR photothermal therapy using polyaniline nanoparticles*. Biomaterials, 2013. **34**(37): p. 9584-9592.
44. Chen, Y., et al., *Pluronic F127-functionalized molybdenum oxide nanosheets with pH-dependent degradability for chemo-photothermal cancer therapy*. Journal of colloid and interface science, 2019. **553**: p. 567-580.
45. Dong, H. and Y. Cao, *Carbon Nanomaterials for Optical Bioimaging and Phototherapy*. Carbon Nanomaterials for Bioimaging, Bioanalysis, and Therapy., 2019: p. 43-62.

46. Estelrich, J. and M.A. Busquets, *Iron oxide nanoparticles in photothermal therapy*. Molecules, 2018. **23**(7): p. 1567.
47. Moreira, A.F., et al., *Gold-core silica shell nanoparticles application in imaging and therapy: A review*. Microporous and Mesoporous Materials, 2018. **270**: p. 168-179.
48. Yin, S. and Y. Asakura, *Recent research progress on mixed valence state tungsten based materials*. Tungsten, 2019. **1**(1): p. 5-18.
49. Zhou, M., M. Tian, and C. Li, *Copper-based nanomaterials for cancer imaging and therapy*. Bioconjugate chemistry, 2016. **27**(5): p. 1188-1199.
50. Huang, X., et al., *Gold nanoparticles: interesting optical properties and recent applications in cancer diagnostics and therapy*. 2007.
51. Li, N., P. Zhao, and D. Astruc, *Anisotropic gold nanoparticles: synthesis, properties, applications, and toxicity*. Angewandte Chemie International Edition, 2014. **53**(7): p. 1756-1789.
52. Greish, K., *Enhanced permeability and retention (EPR) effect for anticancer nanomedicine drug targeting*, in *Cancer nanotechnology*. 2010, Springer. p. 25-37.
53. Chen, J., et al., *Nanomaterials as photothermal therapeutic agents.* Progress in materials science, 2019. **99**: p. 1-26.
54. Singh, R. and J.W. Lillard Jr, *Nanoparticle-based targeted drug delivery*. Experimental and molecular pathology, 2009. **86**(3): p. 215-223.
55. Moghimi, S.M., A.C. Hunter, and J.C. Murray, *Long-circulating and target-specific nanoparticles: theory to practice*. Pharmacological reviews, 2001. **53**(2): p. 283-318.
56. Wang, B., et al., *Metabolism of nanomaterials in vivo: blood circulation and organ clearance.* Accounts of chemical research, 2013. **46**(3): p. 761-769.
57. Jain, R.K. and T. Stylianopoulos, *Delivering nanomedicine to solid tumors*. Nature reviews Clinical oncology, 2010. **7**(11): p. 653.
58. Matsumoto, Y., et al., *Vascular bursts enhance permeability of tumour blood vessels and improve nanoparticle delivery*. Nature nanotechnology, 2016. **11**(6): p. 533.
59. Lamprecht, A., et al., *Biodegradable nanoparticles for targeted drug delivery in treatment of inflammatory bowel disease.* Journal of Pharmacology and Experimental Therapeutics, 2001. **299**(2): p. 775-781.
60. Heo, D.N., et al., *Gold nanoparticles surface-functionalized with paclitaxel drug and biotin receptor as theranostic agents for cancer therapy*. Biomaterials, 2012. **33**(3): p. 856-866.

61. Chitgupi, U., Y. Qin, and J.F. Lovell, *Targeted nanomaterials for phototherapy*. Nanotheranostics, 2017. **1**(1): p. 38.
62. Sunoqrot, S., et al., *Prolonged blood circulation and enhanced tumor accumulation of folate-targeted dendrimer-polymer hybrid nanoparticles*. Journal of controlled release, 2014. **191**: p. 115-122.
63. Yoo, J.-W., E. Chambers, and S. Mitragotri, *Factors that control the circulation time of nanoparticles in blood: challenges, solutions and future prospects*. Current pharmaceutical design, 2010. **16**(21): p. 2298-2307.
64. Van Hong Nguyen, B.-J.L., *Protein corona: a new approach for nanomedicine design*. International journal of nanomedicine, 2017. **12**: p. 3137.
65. Nel, A.E., et al., *Understanding biophysicochemical interactions at the nano–bio interface*. Nature materials, 2009. **8**(7): p. 543-557.
66. Li, X., et al., *The systematic evaluation of size-dependent toxicity and multi-time biodistribution of gold nanoparticles*. Colloids and Surfaces B: Biointerfaces, 2018. **167**: p. 260-266.
67. Larsen, E.K., et al., *Size-dependent accumulation of PEGylated silane-coated magnetic iron oxide nanoparticles in murine tumors*. ACS nano, 2009. **3**(7): p. 1947-1951.
68. Liu, Y., et al., *A plasmonic gold nanostar theranostic probe for in vivo tumor imaging and photothermal therapy*. Theranostics, 2015. **5**(9): p. 946.
69. Perrault, S.D., et al., *Mediating tumor targeting efficiency of nanoparticles through design*. Nano letters, 2009. **9**(5): p. 1909-1915.
70. Ernsting, M.J., et al., *Factors controlling the pharmacokinetics, biodistribution and intratumoral penetration of nanoparticles*. Journal of Controlled Release, 2013. **172**(3): p. 782-794.
71. Li, S.-D. and L. Huang, *Pharmacokinetics and biodistribution of nanoparticles*. Molecular pharmaceutics, 2008. **5**(4): p. 496-504.
72. Li, S.-D. and L. Huang, *Nanoparticles evading the reticuloendothelial system: role of the supported bilayer*. Biochimica et Biophysica Acta (BBA)-Biomembranes, 2009. **1788**(10): p. 2259-2266.
73. Wang, M. and M. Thanou, *Targeting nanoparticles to cancer*. Pharmacological research, 2010. **62**(2): p. 90-99.
74. Sharker, S.M., et al., *Functionalized biocompatible WO3 nanoparticles for triggered and targeted in vitro and in vivo photothermal therapy*. Journal of Controlled Release, 2015. **217**: p. 211-220.

75. Xuan, M., et al., *Macrophage cell membrane camouflaged Au nanoshells for in vivo prolonged circulation life and enhanced cancer photothermal therapy*. ACS applied materials & interfaces, 2016. **8**(15): p. 9610-9618.
76. Rodrigues, C.F., et al., *Functionalization of AuMSS nanorods towards more effective cancer therapies*. Nano Research, 2019. **12**(4): p. 719-732.
77. Amendola, V., et al., *Surface plasmon resonance in gold nanoparticles: a review*. Journal of Physics: Condensed Matter, 2017. **29**(20): p. 203002.
78. Jaque, D., et al., *Nanoparticles for photothermal therapies*. nanoscale, 2014. **6**(16): p. 9494-9530.
79. Li, J.-L. and M. Gu, *Gold-nanoparticle-enhanced cancer photothermal therapy*. IEEE Journal of selected topics in quantum electronics, 2009. **16**(4): p. 989-996.
80. Huang, X., et al., *Plasmonic photothermal therapy (PPTT) using gold nanoparticles*. Lasers in medical science, 2008. **23**(3): p. 217.
81. Bagley, A.F., et al., *Plasmonic photothermal heating of intraperitoneal tumors through the use of an implanted near-infrared source*. ACS nano, 2013. **7**(9): p. 8089-8097.
82. de Melo-Diogo, D., et al., *Strategies to Improve Cancer Photothermal Therapy Mediated by Nanomaterials*. Advanced Healthcare Materials, 2017. **6**(10).
83. Moreira, A.F., et al., *Poly (vinyl alcohol)/chitosan layer-by-layer microneedles for cancer chemo-photothermal therapy*. International Journal of Pharmaceutics, 2020. **576**: p. 118907.
84. Rodrigues, C.F., et al., *Optimization of gold core-mesoporous silica shell functionalization with TPGS and PEI for cancer therapy*. Microporous and Mesoporous Materials, 2019. **285**: p. 1-12.
85. Yao, C., et al., *Gold nanoparticle mediated phototherapy for cancer*. Journal of Nanomaterials, 2016. **2016**.
86. Amendoeira, A., et al., *Light Irradiation of Gold Nanoparticles Toward Advanced Cancer Therapeutics*. Advanced Therapeutics, 2020. **3**(1): p. 1900153.
87. Lopes, T.S., et al., *Advances and potential application of gold nanoparticles in nanomedicine*. Journal of cellular biochemistry, 2019. **120**(10): p. 16370-16378.
88. Zhao, P., N. Li, and D. Astruc, *State of the art in gold nanoparticle synthesis*. Coordination Chemistry Reviews, 2013. **257**(3-4): p. 638-665.
89. Reis, C.A., et al., *Development of gold-core silica shell nanospheres coated with poly-2-ethyl-oxazoline and β-cyclodextrin aimed for cancer therapy*. Materials Science and Engineering: C, 2019. **98**: p. 960-968.
90. Xia, Y. and N.J. Halas, *Shape-controlled synthesis and surface plasmonic properties of metallic nanostructures*. MRS bulletin, 2005. **30**(5): p. 338-348.

91. Blakey, I., Z. Merican, and K.J. Thurecht, *A method for controlling the aggregation of gold nanoparticles: tuning of optical and spectroscopic properties*. Langmuir, 2013. **29**(26): p. 8266-8274.
92. Link, S. and M.A. El-Sayed, *Size and temperature dependence of the plasmon absorption of colloidal gold nanoparticles*. The Journal of Physical Chemistry B, 1999. **103**(21): p. 4212-4217.
93. Link, S. and M.A. El-Sayed, *Spectral properties and relaxation dynamics of surface plasmon electronic oscillations in gold and silver nanodots and nanorods*. 1999, ACS Publications.
94. Jain, P.K., I.H. El-Sayed, and M.A. El-Sayed, *Au nanoparticles target cancer*. nano today, 2007. **2**(1): p. 18-29.
95. Sun, Y. and Y. Xia, *Gold and silver nanoparticles: a class of chromophores with colors tunable in the range from 400 to 750 nm*. Analyst, 2003. **128**(6): p. 686-691.
96. Reinhard, B.M., et al., *Calibration of dynamic molecular rulers based on plasmon coupling between gold nanoparticles*. Nano letters, 2005. **5**(11): p. 2246-2252.
97. Jain, P.K., W. Huang, and M.A. El-Sayed, *On the universal scaling behavior of the distance decay of plasmon coupling in metal nanoparticle pairs: a plasmon ruler equation*. Nano Letters, 2007. **7**(7): p. 2080-2088.
98. Jain, P.K. and M.A. El-Sayed, *Universal scaling of plasmon coupling in metal nanostructures: extension from particle pairs to nanoshells*. Nano letters, 2007. **7**(9): p. 2854-2858.
99. Kottmann, J.P. and O.J. Martin, *Plasmon resonant coupling in metallic nanowires*. Optics Express, 2001. **8**(12): p. 655-663.
100. Sweatlock, L., et al., *Highly confined electromagnetic fields in arrays of strongly coupled Ag nanoparticles*. Physical Review B, 2005. **71**(23): p. 235408.
101. Li, H., et al., *Combination of active targeting, enzyme-triggered release and fluorescent dye into gold nanoclusters for endomicroscopy-guided photothermal/photodynamic therapy to pancreatic ductal adenocarcinoma*. Biomaterials, 2017. **139**: p. 30-38.
102. Park, S., et al., *Gold nanocluster-loaded hybrid albumin nanoparticles with fluorescence-based optical visualization and photothermal conversion for tumor detection/ablation*. Journal of Controlled Release, 2019. **304**: p. 7-18.
103. Wang, M., et al., *Gold nanoshell coated thermo-pH dual responsive liposomes for resveratrol delivery and chemo-photothermal synergistic cancer therapy*. Journal of Materials Chemistry B, 2017. **5**(11): p. 2161-2171.

104. Manivasagan, P., et al., *Anti-EGFR antibody conjugated thiol chitosan-layered gold nanoshells for dual-modal imaging-guided cancer combination therapy*. Journal of controlled release, 2019. **311**: p. 26-42.
105. Ben-Yakar, A., D. Eversole, and O. Ekici, *Spherical and anisotropic gold nanomaterials in plasmonic laser phototherapy of cancer*. Nanotechnologies for the Life Sciences: Online, 2007.
106. Lee, K.-S. and M.A. El-Sayed, *Dependence of the enhanced optical scattering efficiency relative to that of absorption for gold metal nanorods on aspect ratio, size, end-cap shape, and medium refractive index*. The Journal of Physical Chemistry B, 2005. **109**(43): p. 20331-20338.
107. Huang, X. and M.A. El-Sayed, *Gold nanoparticles: Optical properties and implementations in cancer diagnosis and photothermal therapy*. Journal of advanced research, 2010. **1**(1): p. 13-28.
108. Mackey, M.A., et al., *The most effective gold nanorod size for plasmonic photothermal therapy: theory and in vitro experiments*. The Journal of Physical Chemistry B, 2014. **118**(5): p. 1319-1326.
109. Zhang, W., et al., *pH and near-infrared light dual-stimuli responsive drug delivery using DNA-conjugated gold nanorods for effective treatment of multidrug resistant cancer cells*. Journal of Controlled Release, 2016. **232**: p. 9-19.
110. Barbosa, S., et al., *Tuning size and sensing properties in colloidal gold nanostars*. Langmuir, 2010. **26**(18): p. 14943-14950.
111. Khoury, C.G. and T. Vo-Dinh, *Gold nanostars for surface-enhanced Raman scattering: synthesis, characterization and optimization*. The Journal of Physical Chemistry C, 2008. **112**(48): p. 18849-18859.
112. Espinosa, A., et al., *Cancer cell internalization of gold nanostars impacts their photothermal efficiency in vitro and in vivo: toward a plasmonic thermal fingerprint in tumoral environment*. Advanced healthcare materials, 2016. **5**(9): p. 1040-1048.
113. Xia, F., et al., *Matrix metallopeptidase 2 targeted delivery of gold nanostars decorated with IR-780 iodide for dual-modal imaging and enhanced photothermal/photodynamic therapy*. Acta biomaterialia, 2019. **89**: p. 289-299.
114. Feng, Y., et al., *Time-staggered delivery of erlotinib and doxorubicin by gold nanocages with two smart polymers for reprogrammable release and synergistic with photothermal therapy*. Biomaterials, 2019. **217**: p. 119327.
115. Chen, J., et al., *Gold nanocages: bioconjugation and their potential use as optical imaging contrast agents*. Nano letters, 2005. **5**(3): p. 473-477.

116. Huang, S., et al., *Folic-Acid-Mediated Functionalized Gold Nanocages for Targeted Delivery of Anti-miR-181b in Combination of Gene Therapy and Photothermal Therapy against Hepatocellular Carcinoma*. Advanced Functional Materials, 2016. **26**(15): p. 2532-2544.
117. Sun, H., et al., *Cancer cell membrane-coated gold nanocages with hyperthermia-triggered drug release and homotypic target inhibit growth and metastasis of breast cancer*. Advanced Functional Materials, 2017. **27**(3): p. 1604300.
118. Anselmo, A.C. and S. Mitragotri, *Nanoparticles in the clinic*. Bioengineering & translational medicine, 2016. **1**(1): p. 10-29.
119. El-Boubbou, K., *Magnetic iron oxide nanoparticles as drug carriers: clinical relevance*. Nanomedicine, 2018. **13**(8): p. 953-971.
120. Wicki, A., et al., *Nanomedicine in cancer therapy: challenges, opportunities, and clinical applications*. Journal of controlled release, 2015. **200**: p. 138-157.
121. Wolfram, J. and M. Ferrari, *Clinical cancer nanomedicine*. Nano today, 2019.
122. Gil, P.R., et al., *Nanopharmacy: Inorganic nanoscale devices as vectors and active compounds*. Pharmacological research, 2010. **62**(2): p. 115-125.
123. Mahmoudi, K., et al., *Magnetic hyperthermia therapy for the treatment of glioblastoma: a review of the therapy's history, efficacy and application in humans*. International Journal of Hyperthermia, 2018. **34**(8): p. 1316-1328.
124. Grauer, O., et al., *Combined intracavitary thermotherapy with iron oxide nanoparticles and radiotherapy as local treatment modality in recurrent glioblastoma patients*. Journal of neuro-oncology, 2019. **141**(1): p. 83-94.
125. Anselmo, A.C. and S. Mitragotri, *A review of clinical translation of inorganic nanoparticles*. The AAPS journal, 2015. **17**(5): p. 1041-1054.
126. Shi, J., et al., *Cancer nanomedicine: progress, challenges and opportunities*. Nature Reviews Cancer, 2017. **17**(1): p. 20.
127. Oldenburg, S.J., et al., *Current Good Manufacturing Practices (cGMPs) in the Commercial Development of Nanomaterials for Hyperthermia Applications*, in *Nanomaterials for Magnetic and Optical Hyperthermia Applications*. 2019, Elsevier. p. 339-353.
128. Bayda, S., et al., *Inorganic nanoparticles for cancer therapy: a transition from lab to clinic*. Current medicinal chemistry, 2018. **25**(34): p. 4269-4303.
129. oLee, C., et al., *Rabies virus-inspired silica-coated gold nanorods as a photothermal therapeutic platform for treating brain tumors*. Advanced Materials, 2017. **29**(13): p. 1605563.

130. Zhou, H., et al., *Dual targeting hyaluronic acid-RGD mesoporous silica coated gold nanorods for chemo-photothermal cancer therapy*. Materials Science and Engineering: C, 2017. **81**: p. 261-270.
131. Liu, J., et al., *Tumor acidity activating multifunctional nanoplatform for NIR-mediated multiple enhanced photodynamic and photothermal tumor therapy*. Biomaterials, 2018. **157**: p. 107-124.
132. Zhang, Z., et al., *Silver nanoparticle gated, mesoporous silica coated gold nanorods (AuNR@ MS@ AgNPs): low premature release and multifunctional cancer theranostic platform*. ACS applied materials & interfaces, 2015. **7**(11): p. 6211-6219.
133. Luo, G.F., et al., *A Triple-Collaborative Strategy for High-Performance Tumor Therapy by Multifunctional Mesoporous Silica-Coated Gold Nanorods*. Advanced Functional Materials, 2016. **26**(24): p. 4339-4350.
134. Baek, S., et al., *Triple hit with drug carriers: pH-and temperature-responsive theranostics for multimodal chemo-and photothermal therapy and diagnostic applications*. ACS applied materials & interfaces, 2016. **8**(14): p. 8967-8979.
135. Xu, C., et al., *Bacteria-like mesoporous silica-coated gold nanorods for positron emission tomography and photoacoustic imaging-guided chemo-photothermal combined therapy*. Biomaterials, 2018. **165**: p. 56-65.
136. Li, X., et al., *Formation of gold nanostar-coated hollow mesoporous silica for tumor multimodality imaging and photothermal therapy*. ACS applied materials & interfaces, 2017. **9**(7): p. 5817-5827.
137. Gao, Y., et al., *Multifunctional gold nanostar-based nanocomposite: synthesis and application for noninvasive MR-SERS imaging-guided photothermal ablation*. Biomaterials, 2015. **60**: p. 31-41.
138. An, J., et al., *In Vivo Computed Tomography/Photoacoustic Imaging and NIR-Triggered Chemo–Photothermal Combined Therapy Based on a Gold Nanostar-, Mesoporous Silica-, and Thermosensitive Liposome-Composited Nanoprobe*. ACS applied materials & interfaces, 2017. **9**(48): p. 41748-41759.
139. Li, D., et al., *Construction of polydopamine-coated gold nanostars for CT imaging and enhanced photothermal therapy of tumors: an innovative theranostic strategy*. Journal of Materials Chemistry B, 2016. **4**(23): p. 4216-4226.
140. Wei, P., et al., *Dendrimer-Stabilized gold nanostars as a multifunctional theranostic nanoplatform for CT imaging, photothermal therapy, and gene silencing of tumors*. Advanced healthcare materials, 2016. **5**(24): p. 3203-3213.

141. Liu, Y., et al., *Gold nanoshell-based betulinic acid liposomes for synergistic chemo-photothermal therapy*. Nanomedicine: Nanotechnology, Biology and Medicine, 2017. **13**(6): p. 1891-1900.
142. SeokáChung, U., *Dendrimer porphyrin-coated gold nanoshells for the synergistic combination of photodynamic and photothermal therapy*. Chemical communications, 2016. **52**(6): p. 1258-1261.
143. Iodice, C., et al., *Enhancing photothermal cancer therapy by clustering gold nanoparticles into spherical polymeric nanoconstructs*. Optics and Lasers in Engineering, 2016. **76**: p. 74-81.
144. Yang, J., et al., *Spatially confined fabrication of core–shell gold nanocages@ mesoporous silica for near-infrared controlled photothermal drug release*. Chemistry of Materials, 2013. **25**(15): p. 3030-3037.
145. Hu, F., et al., *Double-Walled Au Nanocage/SiO2 nanorattles: integrating SERS imaging, drug delivery and photothermal therapy*. Small, 2015. **11**(8): p. 985-993.
146. Dias, D.R., A.F. Moreira, and I.J. Correia, *The effect of the shape of gold core–mesoporous silica shell nanoparticles on the cellular behavior and tumor spheroid penetration*. Journal of Materials Chemistry B, 2016. **4**(47): p. 7630-7640.
147. Moreira, A.F., et al., *Thermo-and pH-responsive nano-in-micro particles for combinatorial drug delivery to cancer cells*. European Journal of Pharmaceutical Sciences, 2017. **104**: p. 42-51.
148. O'brien, J., et al., *Investigation of the Alamar Blue (resazurin) fluorescent dye for the assessment of mammalian cell cytotoxicity*. European journal of biochemistry, 2000. **267**(17): p. 5421-5426.
149. Chegel, V., et al., *Gold nanoparticles aggregation: drastic effect of cooperative functionalities in a single molecular conjugate*. The Journal of Physical Chemistry C, 2012. **116**(4): p. 2683-2690.
150. Han, H.S., et al., *Gold-nanoclustered hyaluronan nano-assemblies for photothermally maneuvered photodynamic tumor ablation*. ACS nano, 2016. **10**(12): p. 10858-10868.
151. Jacinto, T.A., et al., *Hyaluronic acid and vitamin e polyethylene glycol succinate functionalized gold-core silica shell nanorods for cancer targeted photothermal therapy*. Colloids and Surfaces B: Biointerfaces, 2020. **188**: p. 110778.
152. Mero, A., et al., *Synthesis and characterization of poly (2-ethyl 2-oxazoline)-conjugates with proteins and drugs: suitable alternatives to PEG-conjugates?* Journal of Controlled Release, 2008. **125**(2): p. 87-95.

153. He, Q., et al., *A pH-responsive mesoporous silica nanoparticles-based multi-drug delivery system for overcoming multi-drug resistance*. Biomaterials, 2011. **32**(30): p. 7711-7720.
154. Zeng, Q., et al., *Inhibitation of cellular toxicity of gold nanoparticles by surface encapsulation of silica shell for hepatocarcinoma cell application*. ACS applied materials & interfaces, 2014. **6**(21): p. 19327-19335.
155. Chan, M.-H. and H.-M. Lin, *Preparation and identification of multifunctional mesoporous silica nanoparticles for in vitro and in vivo dual-mode imaging, theranostics, and targeted tracking*. Biomaterials, 2015. **46**: p. 149-158.